Resurrection of plant disease resistance proteins via helper NLR bioengineering

Mauricio P. Contreras[1], Hsuan Pai[1], Muniyandi Selvaraj[1], AmirAli Toghani[1], David M. Lawson[2], Yasin Tumtas[3], Cian Duggan[3], Enoch Lok Him Yuen[3], Clare E. M. Stevenson[2], Adeline Harant[1], Abbas Maqbool[1,‡], Chih-Hang Wu[4], Tolga O. Bozkurt[3], Sophien Kamoun[1,*] and Lida Derevnina[1,†,*]

1: The Sainsbury Laboratory, University of East Anglia, Norwich, United Kingdom.
2: Department of Biochemistry and Metabolism, John Innes Centre, Norwich, United Kingdom.
3: Department of Life Sciences, Imperial College, London, United Kingdom.
4: Institute of Plant and Microbial Biology, Academia Sinica, Taipei, Taiwan.

‡Current address: Department of Biochemistry and Metabolism, John Innes Centre, Norwich, United Kingdom.
†Current address: Crop Science Centre, Department of Plant Sciences, University of Cambridge, Cambridge, United Kingdom.

*Correspondence to: sophien.kamoun@tsl.ac.uk (SK); ld645@cam.ac.uk (LD)

One sentence summary: A helper NLR is mutated to evade inhibition by a parasite effector.

Abstract

Parasites counteract host immunity by suppressing helper NLR proteins that function as central nodes in immune receptor networks. Understanding the mechanisms of immunosuppression can lead to strategies for bioengineering disease resistance. Here, we show that a cyst nematode virulence effector binds and inhibits oligomerization of the helper NLR protein NRC2 by physically preventing intramolecular rearrangements required for activation. A single amino acid polymorphism at the binding interface between NRC2 and the inhibitor is sufficient for this helper NLR to evade immune suppression, thereby restoring the activity of multiple disease resistance genes. This points to a novel strategy for resurrecting disease resistance in crop genomes.

Introduction

The nucleotide binding and leucine-rich repeat (NLR) class of intracellular immune receptors are an important component of innate immunity in plants and animals. They mediate intracellular recognition of pathogens and subsequently initiate an array of immune responses in order to counteract infection (*1, 2*). NLRs can be activated by pathogen-secreted virulence proteins, termed effectors, which pathogens deliver into host cells to modulate host physiology (*2*). A hallmark of plant and animal NLR activation is their oligomerization into higher order immune complexes termed resistosomes or inflammasomes, respectively (*3-9*). These complexes initiate immune signaling via diverse mechanisms, often leading to a form of programmed cell death, termed hypersensitive response (HR) in plants or pyroptosis in animals (*10, 11*). Recent studies have reported NLR-like proteins mediating antiviral immunity and programmed cell death in prokaryotes via mechanisms analogous to those found in eukaryotic NLRs, suggesting that this is a conserved defense mechanism across all three domains of life (*12*). Remarkably, pathogen effectors can act both as triggers and suppressors of NLR-mediated immunity (*13*). In some cases, adapted pathogens deploy effectors which directly or indirectly interfere with NLR signaling to suppress immune activation (*12, 14-17*). However, the exact biochemical mechanisms by which pathogen effectors compromise NLR-mediated immunity to promote disease remain largely unknown. Moreover, whereas multiple strategies to bioengineer novel effector recognition specificities in NLRs have been proposed in recent years (*18*), approaches to mitigate the impact of effector-mediated immune suppression of NLRs are lacking.

NLRs belong to the signal ATPases with numerous domains (STAND) superfamily. They typically exhibit a tripartite domain architecture consisting of an N-terminal signaling domain, a central nucleotide binding domain and C-terminal superstructure forming repeats (*2*). The central domain, termed NB-ARC (nucleotide binding adaptor shared by APAF-1, plant R proteins and CED-4) in plant NLRs, is a hallmark of this protein family and plays a key role as a molecular switch, mediating conformational changes required for activation. NB-ARC domains consist of a nucleotide binding domain (NB), a helical domain (HD1), and a winged-helix domain (WHD) (*2, 19*). Diverse NLR activation and signaling strategies are found in nature. In some cases one NLR protein, termed a singleton, can mediate both elicitor perception and subsequent immune signaling (*20*). However, some NLRs can function as receptor pairs or in higher order configurations termed immune receptor networks (*13, 21*). In these cases, one NLR acts as a pathogen sensor, requiring a second helper NLR to initiate immune signaling. Such is the case in the solanaceous NRC immune receptor network,

64 which is comprised of multiple sensor NLRs that require an array of downstream helper NLRs termed
65 NRCs (NLRs required for cell death) to successfully initiate immune signaling. Upon perception of
66 their cognate effectors, sensors in this network activate oligomerization of their downstream NRC
67 helpers into a putative NRC resistosome, without stably forming part of the mature complex. This
68 has been termed the activation-and release model (*4*). The NRC network can encompass up to half of
69 the NLRome in some solanaceous plant species and plays a key role in mediating immunity against a
70 variety of plant pathogens including oomycetes, bacteria, viruses, nematodes and insects (*15, 21*).
71
72 Plant and metazoan parasites have evolved effectors that interfere with host NLR signaling to promote
73 disease. Parasite effectors can suppress NLR-mediated immunity indirectly by interfering with host
74 proteins that act downstream of NLR signaling (*15, 17, 22, 23*), or directly by interacting with NLRs
75 to inhibit their functions (*15, 16, 24*). One such example is the potato cyst nematode (*Globodera*
76 *rostochiensis*) effector, SPRYSEC15 (SS15), which can suppress signaling mediated by *Nicotiana*
77 *benthamiana* helper NLRs NRC2 and NRC3 and tomato (*Solanum lycopersicum*) helper NLR NRC1, by
78 binding to their central NB-ARC domains (*15*) (**Fig. 1A, Fig. S1A**). In this study, we reasoned that
79 mapping the binding interface between SS15 and its target helper NLRs would enable us to
80 bioengineer NLR variants that evade pathogen suppression, therefore resurrecting the immune
81 signaling activity of upstream sensors in the NRC network.
82

83 **Results**

84 First, we investigated how SS15 binding to NRC2 prevents immune signaling., notably whether SS15
85 prevents oligomerization of NRC following sensor NLR activation. To test this hypothesis, we
86 transiently co-expressed NRC2 or NRC4 with their upstream sensor Rx and the effector SS15 in leaves
87 of *nrc2/3/4* CRISPR KO *N. benthamiana* plants and leveraged previously established BN-PAGE-based
88 readouts for NRC resistosome formation (*4*). For biochemical analyses, we used previously described
89 NRC2 and NRC4 variants with mutations in their N-terminal MADA motifs ($NRC2^{EEE}$ and $NRC4^{AAA}$,
90 respectively) which abolish cell death induction without compromising receptor activation,
91 oligomerization, or localization (*4, 25, 26*). We activated the Rx-NRC system by co-expressing PVX
92 CP-GFP or free GFP as an inactive control. In the absence of SS15, both NRC2 and NRC4
93 oligomerize upon effector-triggered activation mediated by their upstream sensor Rx. However, when
94 SS15 is present, Rx/CP-activated NRC2 is unable to oligomerize and appears as a band of ~240 kDa,
95 which co-migrates with SS15. Inactive NRC2 co-expressed with SS15 also migrates as a band of ~240

96 kDa, which is slower-migrating relative to inactive NRC2 in the absence of SS15, indicative of *in vivo*
97 NRC2-SS15 complex formation (**Fig. 1B, Fig. S1**). We also observed that SS15 co-expression not
98 only blocks NRC2 oligomerization but also prevents the previously reported shift of NRC2 from
99 cytoplasm to PM as well as the formation of NRC2 PM-associated puncta upon Rx/CP activation
100 (**Fig. S2**) (*4*). In contrast, NRC4 oligomerization is not affected in the presence of SS15, which is in
101 line with previous findings that NRC4 immune signaling is not suppressed by SS15 (*15*). We conclude
102 that SS15 can suppress immune signaling by acting as a direct proteinaceous inhibitor of NRC2, but
103 not NRC4, by directly binding to its NB-ARC domain to block the formation of a signal-competent
104 oligomeric resistosome.
105
106 Given that NRC4 retains the capacity to oligomerize in the presence of SS15, we leveraged this
107 differential SS15 sensitivity between NRC2 and NRC4 to identify the domain that determines SS15
108 association and inhibition. We generated a series of NRC2-NRC4 chimeric proteins (**Fig. 2A-2B, Fig.**
109 **S3**), which we subsequently assayed for SS15 association via *in planta* co-immunoprecipitation. We
110 identified one chimeric variant of NRC4, carrying the HD1-1 region of NRC2 ($NRC4^{2HD1-1}$), which
111 gains association to SS15 (**Fig. 2C**). Unlike NRC4, $NRC4^{2HD1-1}$ is susceptible to inhibition by SS15
112 and is unable to oligomerize and trigger cell death in the presence of SS15 (**Fig. 2D-2E, Fig. S3, Fig.**
113 **S4**). We conclude that the HD1-1 region is important for association to SS15 and for the effector to
114 directly inhibit NRC oligomerization and programmed cell death.
115
116 To further define the interface between SS15 and NRC proteins, we crystallized SS15 in complex with
117 the NB-ARC domain of SlNRC1, a tomato NRC that is inhibited by the nematode effector. We
118 subsequently solved the structure using X-ray diffraction data collected to 4.5 Å resolution (**Fig. 3A**,
119 **Fig. S5**, **Table S3**), which allowed us to determine that SS15 binds to a loop in the HD1-1 region of
120 NRCs which connects the NB domain to the HD1 and WHD domains. This provides orthogonal
121 evidence that the SS15-NRC interactions are mediated by this region as shown with the chimera
122 experiments (**Fig. 2**). This loop was previously shown to act as a "hinge", allowing the NB domain to
123 rotate relative to the HD1 and WHD domains following activation (**Fig. S5**, **Movie S1**) (*27*). We
124 propose that SS15 prevents conformational changes that are critical for NLR activation by binding
125 and immobilizing the NB-HD1 hinge.
126

127 Given that SS15 suppresses cell death induction mediated by SlNRC1, NRC2 and NRC3 but not
128 NRC4 or other well characterized NLRs such as ZAR1 (**Fig. S1**) (*15*), we leveraged the high degree
129 of conservation that is characteristic of plant NB-ARC domains to narrow down residues within the
130 binding interface that underpin this interaction. We shortlisted residues within the HD1-1 region that
131 are similar in SlNRC1, NRC2 and NRC3 but different in NRC4 or AtZAR1 (**Fig. 3B**). Combining
132 information from the co-crystal structure and the alignments allowed us to select 13 candidate residues
133 to test by mutagenesis in NRC2 (**Fig. 3B**). We mutated each of these residues to the corresponding
134 amino acid found in NRC4 and screened these NRC2 variants for susceptibility to SS15 inhibition in
135 cell death assays. This revealed two variants, NRC2^{E316P} and NRC2^{D317K} which triggered cell death
136 when activated by Rx/CP and were no longer inhibited by SS15 (**Fig. 3C, Fig. S6, Fig. S7**). We also
137 tested all 13 single amino acid mutants for association with SS15 by *in planta* co-immunoprecipitation
138 and found that NRC2^{E316P} and NRC2^{D317K} exhibited reduced association with SS15 relative to NRC2
139 (**Fig. 3D, Fig. S6**), which is in line with the observation that SS15 is not able to suppress these variants
140 (**Fig. 3C**). We conclude that the E316 and D317 residues are critical for SS15-mediated inhibition of
141 NRC2 and that mutating these residues to their equivalent amino acid in NRC4 allows Rx/CP-
142 activated NRC2 to evade SS15 association and inhibition.
143
144 We next tested whether these two SS15-evading variants of NRC2 could restore functionality of
145 NRC2-dependent sensor NLRs that are suppressed by the parasite effector. We tested this by
146 performing complementation assays with NRC2^{E316P} and NRC2^{D317K} in *nrc2/3/4* CRISPR KO *N.*
147 *benthamiana* plants. We activated the NRC2 variants with a panel of agronomically important sensor
148 NLRs mediating resistance to diverse pathogens, including the potato cyst nematode R gene Gpa2 (an
149 allele of Rx), as well as other well characterized oomycete and bacterial resistance proteins.
150 Remarkably, NRC2^{D317K} evaded SS15 inhibition with all tested sensor NLRs restoring their capacity
151 to activate immune signaling (**Fig 4A**, **Fig. S8, Fig. S9**). In contrast, NRC2^{E316P} could evade SS15
152 suppression when activated by Rx, but not when activated by other sensors. We therefore selected
153 NRC2^{D317K} for follow-up biochemical studies, using BN-PAGE-based assays. Unlike NRC2, activated
154 NRC2^{D317K} oligomerized even in the presence of SS15 and did not form an *in vivo* complex with the
155 inhibitor (**Fig. 4B**). We conclude that NRC2^{D317K} can fully evade SS15-mediated immune suppression,
156 retaining the capacity to oligomerize and mediate cell death when activated by multiple agronomically
157 important sensor NLRs.
158

159 ## Conclusion

160 Our study reveals how a parasite effector has evolved as an inhibitor of a helper NLR by directly
161 binding its NB-ARC domain to prevent resistosome formation and immune signaling. By binding and
162 immobilizing a critical hinge loop in the HD1 region of the NB-ARC, SS15 restricts movement of the
163 NB domain relative to the HD1 and WHD domains, preventing immune receptor activation.
164 Remarkably, while SS15 can bind and inhibit NRC2, it cannot bind or inhibit the NRC2 paralog
165 NRC4. We exploited NRC4's resilience to SS15 inhibition by making chimeric NRC2-NRC4 variants
166 which, together with structural information, helped us identify the inhibitor binding interface.
167 Mutational studies of this interface allowed us to generate a single amino acid variant of NRC2
168 ($NRC2^{D317K}$) that evades SS15 inhibition without compromising receptor signaling capacity. This
169 $NRC2^{D317K}$ variant can now support signaling by any NRC2-dependent sensor even in the presence of
170 SS15.
171
172 The existence of plant parasite secreted NLR inhibitors suggests that suppressed resistance genes may
173 occur in crop genomes. Leveraging the approach detailed in this study, it may be possible to resurrect
174 cryptic or defeated resistance proteins to enhance disease resistance. Moreover, considering that
175 multiple sensors can signal through the same downstream helper, applying this approach to helper
176 NLRs holds potential to simultaneously resurrect multiple upstream sensor NLRs. Importantly, the
177 single amino acid NRC2 variants we identified could in theory be generated in-locus using gene editing
178 technologies in agronomically important crop species, making deployment of this technology viable
179 in countries where transgenic approaches are not feasible. Our work describes a novel approach to
180 achieve robust immunity by engineering NLRs that avoid parasite suppression. This could in theory
181 be applied to other plant, metazoan or even prokaryotic NLR immune receptors that are directly
182 targeted by parasite effectors (*12, 15, 16, 24*). Combined with recent advances in NLR engineering to
183 achieve novel pathogen recognition specificities (*18, 28*), this technology holds the potential to unlock
184 a new era in disease resistance breeding.
185

186 ## Materials and Methods

187 **Plant growth conditions**

188 Wild-type and *nrc2/3/4* CRISPR mutant *Nicotiana benthamiana* lines were grown in a controlled
189 environment growth chamber with a temperature range of 22 to 25 ºC, humidity of 45% to 65% and
190 a 16/8-hour light/dark cycle.

191

192 **Plasmid construction**

193 We used the Golden Gate Modular Cloning (MoClo) kit (*29*) and the MoClo plants part kit (*30*) for
194 cloning. All vectors used were generated with these kits unless otherwise stated. Cloning design and
195 sequence analysis were done using Geneious Prime (v2021.2.2; https://www.geneious.com). Plasmid
196 construction is described in more detail in **Table S1**.

197

198 **Cell death assays by agroinfiltration**

199 Proteins of interest were transiently expressed in *N. benthamiana* according to previously described
200 methods (*31*). Briefly, leaves from 4–5-week-old plants were infiltrated with suspensions
201 of *Agrobacterium tumefaciens* GV3101 pM90 strains transformed with expression vectors coding for
202 different proteins indicated. Final OD_{600} of all *A. tumefaciens* suspensions were adjusted in infiltration
203 buffer (10 mM MES, 10 mM $MgCl_2$, and 150 µM acetosyringone (pH 5.6)). Final OD_{600} used for each
204 construct is described in **Table S2**.

205

206 **Extraction of total proteins for BN-PAGE and SDS-PAGE assays**

207 Four to five-week-old *N. benthamiana* plants were agroinfiltrated as described above with constructs
208 of interest and leaf tissue was collected 3 days post agroinfiltration for NRC2 and 2 days post
209 agroinfiltration for NRC4. Final OD_{600} used for each construct is described in **Table S2**. BN-PAGE
210 was performed using the Bis-Tris Native PAGE system (Invitrogen) according to the manufacturer's
211 instructions, as described previously (*31*). Leaf tissue was ground using a Geno/Grinder tissue
212 homogenizer. For NRC2, GTMN extraction buffer was used (10% glycerol, 50 mM Tris-HCl (pH
213 7.5), 5 mM $MgCl_2$ and 50 mM NaCl) supplemented with 10 mM DTT, 1x protease inhibitor cocktail
214 (SIGMA) and 0.2% Nonidet P-40 Substitute (SIGMA). For NRC4, GHMN buffer (10% glycerol, 50
215 mM HEPES (pH 7.4), 5 mM $MgCl_2$ and 50 mM NaCl) buffer supplemented with 10mM DTT, 1x
216 protease inhibitor cocktail (SIGMA) and 1% Digitonin (SIGMA) was used for extraction. Samples
217 were incubated in extraction buffer on ice for 10 minutes with short vortex mixing every 2 minutes.

218 Following incubation, samples were centrifuged at 5,000 x*g* for 15 minutes and the supernatant was
219 used for BN-PAGE and SDS-PAGE assays.
220
221 **BN-PAGE assays**
222 For BN-PAGE, samples extracted as detailed above were diluted as per the manufacturer's
223 instructions by adding NativePAGE 5% G-250 sample additive, 4x Sample Buffer and water. After
224 dilution, samples were loaded and run on Native PAGE 3%-12% Bis-Tris gels alongside either
225 NativeMark unstained protein standard (Invitrogen) or SERVA Native Marker (SERVA). The
226 proteins were then transferred to polyvinylidene difluoride membranes using NuPAGE Transfer
227 Buffer using a Trans-Blot Turbo Transfer System (Bio-Rad) as per the manufacturer's instructions.
228 Proteins were fixed to the membranes by incubating with 8% acetic acid for 15 minutes, washed with
229 water and left to dry. Membranes were subsequently re-activated with methanol to correctly visualize
230 the unstained native protein marker. Membranes were immunoblotted as described below.
231
232 **SDS-PAGE assays**
233 For SDS-PAGE, samples were diluted in SDS loading dye and denatured at 72 ºC for 10 minutes.
234 Denatured samples were spun down at 5,000 x*g* for 3 minutes and supernatant was run on 4%-20%
235 Bio-Rad 4%-20% Mini-PROTEAN TGX gels alongside a PageRuler Plus prestained protein ladder
236 (Thermo Scientific). The proteins were then transferred to polyvinylidene difluoride membranes using
237 Trans-Blot Turbo Transfer Buffer using a Trans-Blot Turbo Transfer System (Bio-Rad) as per the
238 manufacturer's instructions. Membranes were immunoblotted as described below.
239
240 **Immunoblotting and detection of BN-PAGE and SDS-PAGE assays**
241 Blotted membranes were blocked with 5% milk in Tris-buffered saline plus 0.01% Tween 20 (TBS-T)
242 for an hour at room temperature and subsequently incubated with desired antibodies at 4 ºC overnight.
243 Antibodies used were anti-GFP (B-2) HRP (Santa Cruz Biotechnology), anti-HA (3F10) HRP
244 (Roche), anti-Myc (9E10) HRP (Roche), and anti-V5 (V2260) HRP (Roche), all used in a 1:5000
245 dilution in 5% milk in TBS-T. To visualize proteins, we used Pierce ECL Western (32106, Thermo
246 Fisher Scientific), supplementing with up to 50% SuperSignal West Femto Maximum Sensitivity
247 Substrate (34095, Thermo Fishes Scientific) when necessary. Membrane imaging was carried out with
248 an ImageQuant LAS 4000 or an ImageQuant 800 luminescent imager (GE Healthcare Life Sciences,
249 Piscataway, NJ). Rubisco loading control was stained using Ponceau S (Sigma).

250 **Co-Immunoprecipitation assays**

251 CoIP assays were performed as described previously (*32*). Total soluble protein was extracted as
252 described above from leaves of *N. benthamiana* 3 days post agro-infiltration using GTEN buffer
253 (10% Glycerol, 25 mM Tris-HCl (pH 7.5), 1mM EDTA, 150 mM NaCl) supplemented with 2%
254 (w/v) polyvinylpolypyrrolidone, 10 mM DTT and 1x protease inhibitor cocktail (SIGMA), 0.3%
255 IGEPAL (SIGMA). OD_{600} used can be found in **Table S2**. Protein extracts were filtered using
256 Minisart 0.45 µm filter (Sartorius Stedim Biotech, Goettingen, Germany). Part of the extract was set
257 aside prior to immunoprecipitation and used for SDS-PAGE as described above. These were the
258 inputs. 1.4 ml of the remaining filtered total protein extract was mixed with 30 µl of anti-c-Myc
259 agarose beads (A7470, SIGMA) and incubated end over end for 90 minutes at 4 ºC. Beads were
260 washed 5 times with immunoprecipitation wash buffer (GTEN extraction buffer with 0.3% v/v
261 IGEPAL (SIGMA)) and resuspended in 60 µl of SDS loading dye. Proteins were eluted from beads
262 by heating for 10 minutes at 72 ºC. Immunoprecipitated samples were used for SDS-PAGE and
263 immunoblotted as described above and compared to the inputs.

264

265 **Confocal microscopy**

266 Three to four-week-old plants were agroinfiltrated as described above with constructs of interest. Final
267 OD_{600} used for each construct is described in **Table S2**. Leaf tissue was prepared for imaging by
268 sectioning of desired area surrounding an infiltration spot using a cork borer size 4, and were mounted,
269 live, in wells containing dH2O made in Carolina Observation Gel to enable diffusion of gasses. The
270 abaxial of the leaf tissue was imaged using a Leica SP8 with 40x water immersion objective. Laser
271 excitations for fluorescent proteins were used as described previously (*33*), namely 488 nm (Argon)
272 for GFP, 561/594 nm (Diode) for RFP and 405 nm (Diode) for BFP.

273

274 **Membrane enrichment assays**

275 Membrane enrichment was carried out by slightly modifying a previously described protocol (*34*). In
276 brief, leaf material was ground to fine powder using liquid nitrogen and 2x volume of extraction buffer
277 was added. Extraction buffer consisted of 0.81M sucrose, 5% (v/v) glycerol, 10 mM EDTA, 10 mM
278 EGTA, 5mM KCl, and 100 mM Tris-HCl (pH 7.5) supplemented with 5 mM DTT, 1% Sigma Plant
279 Protease Inhibitor Cocktail, 1 mM PMSF and 0.5% PVPP. After addition of the buffer, the samples
280 were vortexed for a minute and the cell debris was cleared out by two subsequent centrifugation steps
281 at 1000 xg for 5 min. The supernatant was diluted 1:1 using distilled water and an aliquot of the

282 supernatant was separated as the total fraction (T). The remaining supernatant (200-300 μL) was
283 further centrifuged at 21,000 xg for 90 min at 4°C. This centrifugation yielded the supernatant (soluble
284 fraction, S) and membrane enriched pellet (membrane fraction, M). After separating the soluble
285 fraction, the pellet was resuspended in diluted extraction buffer (without PVPP). All the fractions were
286 diluted with SDS loading dye, and proteins were denatured by incubating at 50°C for 15 min. Western
287 blotting was performed as previously described following SDS-PAGE. Endogenous plasma
288 membrane ATPase was detected using anti-H+ATPase (AS07 260) antibody (Agrisera) as a marker to
289 show the success of membrane enrichment.
290
291 **Heterologous protein production and purification from *E. coli***
292 Heterologous production and purification of SS15 was performed as previously described (*32*).
293 Recombinant SS15 protein (lacking signal peptide) was expressed by cloning in pOPIN-S3C plasmid,
294 with an N-terminal tandem 6xHis-SUMO followed by a 3C protease cleavage site. pOPIN-S3C:SS15
295 was transformed into *E. coli* SHuffle cells. 8L of these cells were grown at 30 ºC in autoinduction
296 media (*35*) to an OD600 of 0.6 to 0.8 followed by overnight incubation at 18 ºC and harvested by
297 centrifugation. Pelleted cells were resuspended in 50 mM Tris HCl (pH 8), 500 mM NaCl, 50 mM
298 Glycine, 5% (vol/vol) glycerol and 20 mM imidazole (buffer A) supplemented with cOmplete EDTA-
299 free protease inhibitor tablets (Roche) and lysed by sonication. The clarified cell lysate was applied to
300 a Ni^{2+}-NTA column connected to an AKTA pure system. 6xHis-SUMO-SS15 was step eluted with
301 elution buffer (buffer A with 500 mM imidazole) and directly injected onto a Superdex 200 26/600
302 gel filtration column pre-equilibrated with buffer B (20 mM HEPES (pH 7.5), 150 mM NaCl). The
303 fractions containing 6xHis-SUMO-SS15 were pooled, and the N-terminal 6xHis-SUMO tag was
304 cleaved by addition of 3C protease (10 μg/mg of fusion protein), incubating overnight at 4ºC. Cleaved
305 SS15 was further purified using a Ni^{2+}-NTA column, this time collecting the flow through to separate
306 the cleaved tag from the SS15 protein. Un-tagged SS15 was further purified by another round of gel
307 filtration as described above. The concentration of protein was judged by absorbance at 280 nm (using
308 a calculated molar extinction coefficient of 35920 M^{-1cm-1} for SS15).
309
310 Heterologous production and purification of $SlNRC1^{NB-ARC}$ was performed as previously described
311 (*36*). Recombinant $SlNRC1^{NB-ARC}$ protein was also expressed cloning in pOPIN-S3C plasmid as
312 described above. pOPIN-S3C:$SlNRC1^{NB-ARC}$ was transformed into *E. coli* Lemo21 (DE3) cells. 8L of
313 these cells were grown at 37 ºC in autoinduction media (*35*) to an OD600 of 0.6 to 0.8 followed by

314 overnight incubation at 18 ºC and harvested by centrifugation. Pelleted cells were resuspended in 50
315 mM Tris HCl (pH 8), 500 mM NaCl, 50 mM Glycine, 5% (vol/vol) glycerol and 20 mM imidazole
316 (buffer A) supplemented with cOmplete EDTA-free protease inhibitor tablets (Roche) and lysed by
317 sonication. The clarified cell lysate was applied to a Ni^{2+}-NTA column connected to an AKTA pure
318 system. 6xHis-SUMO-SlNRC1^{NB-ARC} was step eluted with elution buffer (buffer A with 500 mM
319 imidazole) and directly injected onto a Superdex 200 26/600 gel filtration column pre-equilibrated
320 with buffer B (20 mM HEPES (pH 7.5), 150 mM NaCl). The fractions containing 6xHis-SUMO-
321 SlNRC1^{NB-ARC} were pooled, and the N-terminal 6xHis-SUMO tag was cleaved by addition of 3C
322 protease (10 μg/mg of fusion protein), incubating overnight at 4ºC. Cleaved SlNRC1^{NB-ARC} was further
323 purified using a Ni^{2+}-NTA column, this time collecting the flow through to separate the cleaved tag
324 from the SlNRC1^{NB-ARC} protein. Un-tagged SlNRC1^{NB-ARC} was further purified by another round of gel
325 filtration as described above. The concentration of protein was judged by absorbance at 280 nm (using
326 a calculated molar extinction coefficient of 63370 M^{-1cm-1} for SlNRC1^{NB-ARC}).
327
328 To obtain SlNRC1^{NB-ARC} in complex with SS15, both proteins were incubated in a 1:1 molar ratio
329 overnight at 4 ºC and subjected to gel filtration on a Superdex 200 26/600 gel filtration column as
330 described above. The fractions containing SlNRC1^{NB-ARC} in complex with SS15 were pooled,
331 concentrated to 10-15 mg/ml and subsequently used for crystallisation screens.
332
333 **Crystallisation, data collection, and structure solution**
334 Crystallisation screens were performed at 18°C using the sitting-drop vapour diffusion technique.
335 Drops composed of 0.3 μL of protein solution and 0.3 μL of reservoir solution were set up in MRC
336 96-well crystallisation plates (Molecular Dimensions), which were dispensed using an Oryx Nano or
337 an Oryx8 robot (Douglas Instruments). Crystal growth was monitored using a Minstrel Desktop
338 Crystal Imaging System (Rikagu). Suitable crystals grew after 72 hrs in a Morpheus screen
339 crystallisation condition containing 0.1M MES buffer (pH 6.5), 10% (w/v) PEG8000 and 20% (v/v)
340 ethylene glycol (Molecular Dimensions) and were harvested by flash-cooling in liquid nitrogen using
341 LithoLoops (Molecular Dimensions). X-ray diffraction data were collected at the Diamond Light
342 Source (Didcot, UK) on beamline I03 using an Eiger2 XE 16M pixel array detector (Dectris) with
343 crystals maintained at 100 K by a Cryojet cryocooler (Oxford Instruments).
344 X-ray data were integrated, and scaled using XDS (*37*), as implemented through the XIA2 (*38*)
345 pipeline, and then merged using AIMLESS (*39*), via the CCP4i2 graphical user interface (*40*). The

346 NRC1$^{NB\text{-}ARC}$-SS15 complex crystallised in space group $P6_1$ with cell parameters a=b=128.6, c=170.7 Å,
347 and the best crystal yielded diffraction data to 4.5 Å resolution (see **Table S3** for a summary of data
348 collection and refinement statistics). Given the small size of the dataset, we assigned 10% of the data
349 (883 unique reflections) for the R_{free} calculation, to give a more statistically meaningful metric. The
350 crystal structure of NRC1$^{NB\text{-}ARC}$ alone was already available (PDB 6S2P), but there was no
351 experimentally determined structure for SS15. Thus, we made use of AlphaFold2-multimer (*41*), as
352 implemented through Colabfold
353 (https://colab.research.google.com/github/sokrypton/ColabFold/blob/main/AlphaFold2.ipynb)
354 (*42*) to generate structural predictions for the complex. There was very good sequence coverage for
355 both proteins and the five independent models of the individual components were closely similar. The
356 pLDDT scores were generally good (e.g. averages of 82 and 75 for NRC1$^{NB\text{-}ARC}$ and SS15 models,
357 respectively, from the rank 1 predictions). However, the relative placement of the two components
358 varied across the five models and the corresponding PAE scores indicated very low confidence in
359 these predictions. A comparison of the five NRC1$^{NB\text{-}ARC}$ models with the known crystal structure
360 showed a good agreement (e.g. superposition of the rank 1 model gave an rmsd of 1.77 Å). Given that
361 the AlphaFold2 (AF2) model provided starting coordinates for several loops missing from the crystal
362 structure, we decided to use this model in molecular replacement. Templates for both components
363 were prepared using the "Process Predicted Models" CCP4i2 task, which removed low confidence
364 regions (based on pLDDT) and converted the pLDDT scores in the *B*-factor field of the PDB
365 coordinate files to pseudo *B*-factors. Analysis of the likely composition of the asymmetric unit (ASU)
366 suggested that it contained two copies of each component, giving an estimated solvent content of
367 ~67%. PHASER (*43*) was able to place the four chains within the ASU, although the second SS15
368 domain required manual repositioning with respect to its neighbouring NRC1 domain in order to
369 avoid a number of clashes and improve the fit to the density. This was achieved using COOT (*44*)
370 and guided by the arrangement of the other NRC1-SS15 complex (**Fig. S4**). The structure was then
371 subjected to jelly body refinement in REFMAC5 (*45*) using ProSMART restraints (*46*) generated from
372 the AF2 models, giving R_{work} and R_{free} values of 0.357 and 0.401, respectively, to 4.5 Å resolution.
373
374 Now it was possible to generate more complete models for the components by superposing the
375 original unprocessed AF2 models and trimming these with reference to the improved electron density.
376 Furthermore, a significant region of positive difference density was present at the cores of both NRC1
377 domains, which corresponded to the ADP in the crystal structure; thus we incorporated ADP into the

378 model. Due to the low resolution of the dataset, only very limited rebuilding was possible in COOT,
379 where Geman-McClure and Ramachandran restraints were used to maintain good stereochemical
380 parameters. After several cycles of restrained refinement in REFMAC5 and editing in COOT, a
381 reasonable model was obtained with R_{work} and R_{free} values of 0.258 and 0.298, respectively. However,
382 there remained a region of positive difference density near the N-termini of both SS15 domains that
383 we could not adequately explain. At this point we re-ran the AlphaFold2-multimer predictions, but
384 this time with one copy of the complex taken from the crystal structure as a reference template.
385 Although the new predictions did not produce complexes that were consistent with the X-ray data,
386 and the models for the individual components did not appear to be noticeably improved based on
387 pLDDT scores, we used them as starting points to rebuild the X-ray structure.
388
389 Significantly, for several models, the N-terminal region of SS15 adopted conformations that partially
390 accounted for the region of positive difference density electron density, and this could be improved
391 by careful rebuilding and refinement. This "AlphaFold recycling" procedure was repeated a further
392 two times before finalising the structure, which included residues 153-494 for SlNRC1 (numbered
393 with respect to full length protein) and residues 18-223 for SS15, where residues 33-43 in both copies
394 of the latter formed α-helices that occupied the regions of positive difference density observed earlier.
395 For the last refinement in REFMAC5, the following options were used: ProSMART restraints
396 generated from the latest AF2 models, overall *B*-factor refinement with TLS restraints (where each
397 protein chain was treated as a separate domain), and non-crystallographic symmetry restraints. The
398 final model gave R_{work} and R_{free} values of 0.237 and 0.275, respectively, to 4.5 Å resolution (see **Table**
399 **S3** for a summary of refinement statistics). All structural figures were prepared using ChimeraX (*47*)
400 and PyMOL (*48*).
401

402 **Figures:**

403 **Figure 1**

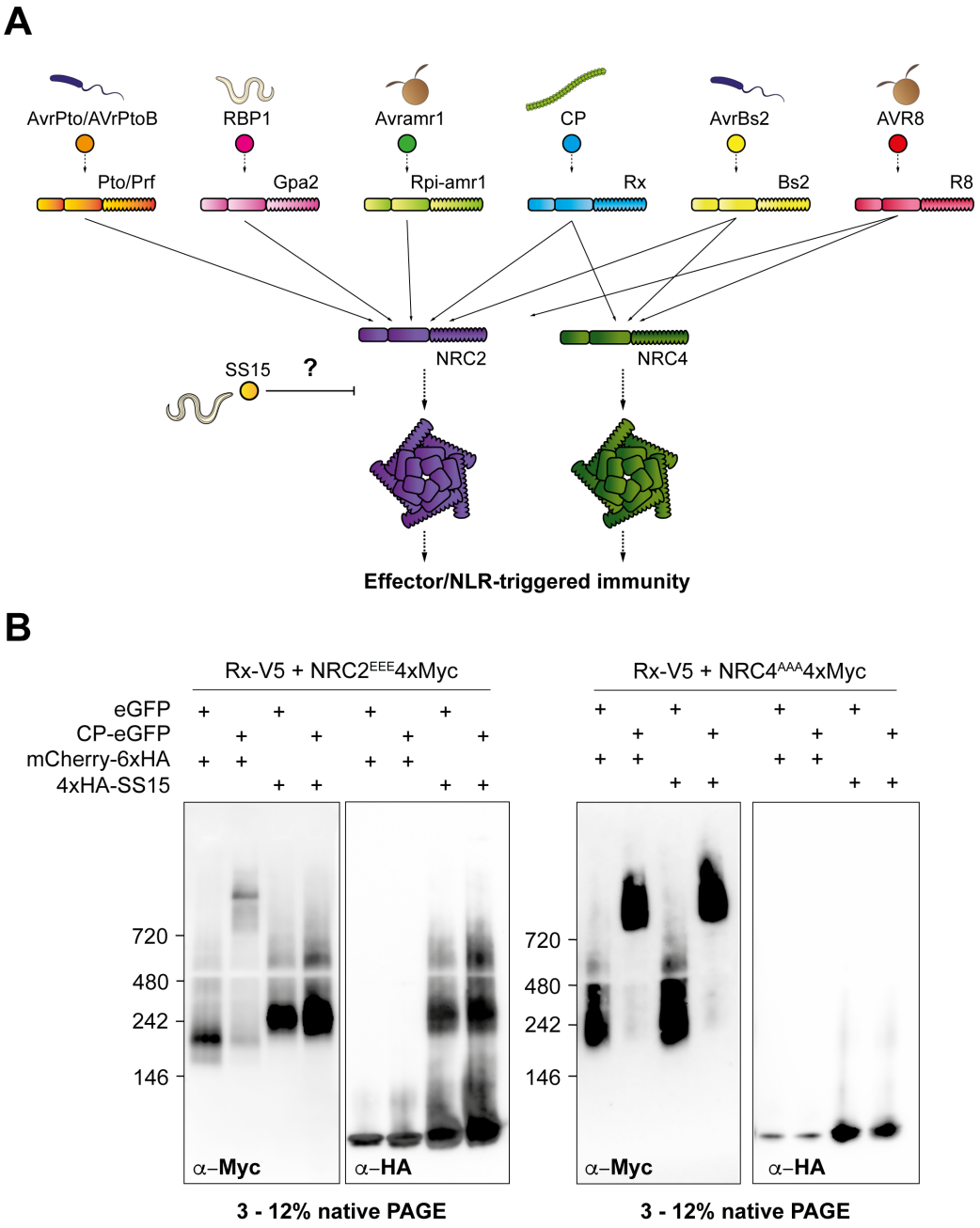

404

405 **Fig. 1: SS15 directly inhibits NRC2, but not NRC4 oligomerization.**

406 (**A**) Schematic representation of the NRC immune receptor network, consisting of multiple sensor
407 NLRs (in blue) and their downstream helper NLRs, NRC2 and NRC4 (in purple and green,
408 respectively). Effector-triggered activation of a sensor leads to downstream helper oligomerization
409 and resistosome formation. The *G. rostochiensis* effector SS15 (in yellow) can directly bind to the NB-

410 ARC domain of NRC2 but not NRC4, thereby inhibiting signaling by directly binding to the NB-ARC
411 domain of this helper NLR. (**B**) BN-PAGE assays with inactive and activated Rx together with NRC2
412 or NRC4, in the absence or presence of SS15. C-terminally V5-tagged Rx and C-terminally 4xMyc-
413 tagged $NRC2^{EEE}$ or $NRC4^{AAA}$ were co-expressed with either free GFP or C-terminally GFP-tagged
414 PVX CP. These effector-sensor-helper combinations were co-infiltrated together with a 6xHA-
415 mCherry fusion protein or with N-terminally 6xHA-tagged SS15. Total protein extracts were run in
416 parallel on native and denaturing PAGE assays and immunoblotted with the appropriate antisera
417 labelled below. Approximate molecular weights (kDa) of the proteins are shown on the left.
418 Corresponding SDS-PAGE assays can be found in **Fig. S1**. The experiment was repeated three times
419 with similar results.
420

421 **Figure 2**

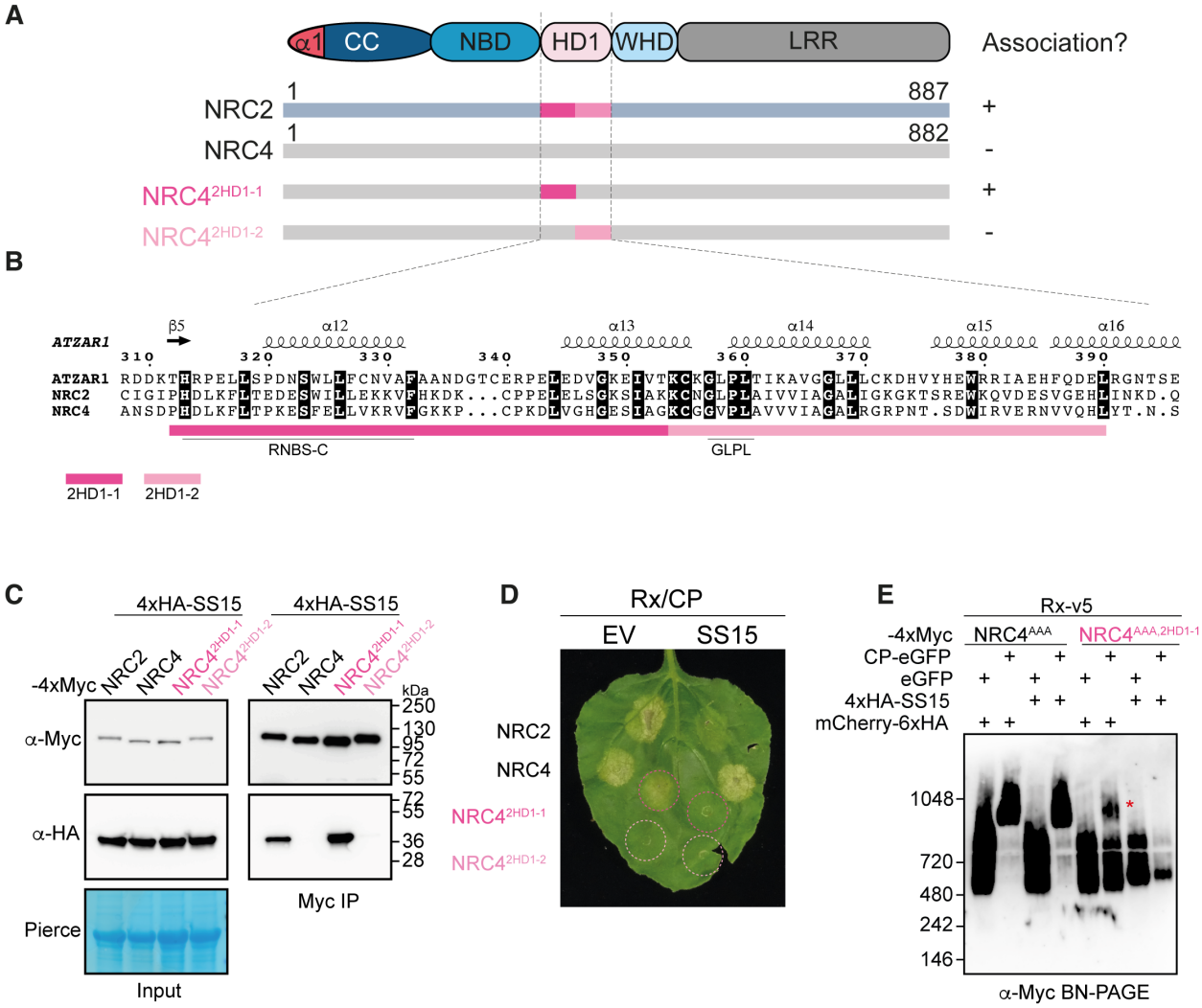

422

423 **Fig. 2: The HD1-1 region of NRC NB-ARC domains determines sensitivity to SS15.**

424 **(A)** Schematic representation of NRC domain architecture, highlighting regions within the NB-ARC
425 domain swapped between NRC2-NRC4 chimeric proteins, namely NRC4^{2HD1-1} and NRC4^{2HD1-2}.
426 Association (+) or lack thereof (-) between these NLR immune receptors and SS15 determined by *in*
427 *planta* co-immunoprecipitation is detailed on the right. (**B**) Close-up view of amino acid sequence
428 alignment between AtZAR1, NRC2 and NRC4 focused on the HD1 region of NB-ARC domain.
429 Predicted secondary structure is shown above the alignment. Well-characterized motifs within this
430 region, such as RNBS-C and GLPL are underlined below the alignment. (**C**) Co-Immunoprecipitation
431 (Co-IP) assays between SS15 and chimeric NRC2-NRC4 variants. C-terminally 4xMyc-tagged NRC
432 proteins were transiently co-expressed with N-terminally 4xHA-tagged SS15. IPs were performed with
433 agarose beads conjugated to Myc antibodies (Myc IP). Total protein extracts were immunoblotted

434 with the appropriate antisera labelled on the left. Approximate molecular weights (kDa) of the proteins
435 are shown on the right. Rubisco loading control was carried out using Ponceau stain (PS). The
436 experiment was repeated three times with similar results. (**D**) Photo of representative leaves from *N.*
437 *benthamiana nrc2/3/4* KO plants showing HR after co-expression of Rx and PVX CP with NRC2,
438 NRC4 and the two NRC2-NRC4 chimeras, $NRC4^{2HD1-1}$ and $NRC4^{2HD1-2}$. These effector-sensor-helper
439 combinations were co-expressed with a free mCherry-6xHA fusion protein (EV) or with N-terminally
440 4xHA-tagged SS15. The experiment consisted of 3 biological replicates with at least 6 technical
441 replicates each. A quantitative analysis of the HR phenotypes can be found in **Fig. S4**. (**E**) BN-PAGE
442 assay with inactive and activated Rx together with NRC4 or an NRC2-NRC4 chimeric protein in the
443 absence or presence of SS15. C-terminally V5-tagged Rx and C-terminally 4xMyc-tagged $NRC4^{AAA}$ or
444 $NRC4^{AAA-2HD1-1}$ were co-expressed with either free GFP or C-terminally GFP-tagged PVX CP. These
445 effector-sensor-helper combinations were co-infiltrated together with a mCherry-6xHA fusion protein
446 or with N-terminally 4xHA-tagged SS15. Total protein extracts were run in parallel on native and
447 denaturing PAGE assays and immunoblotted with the appropriate antisera labelled on the left.
448 Corresponding SDS-PAGE blots can be found in **Fig. S3**. Approximate molecular weights (kDa) of
449 the proteins are shown on the left. The experiment was repeated three times with similar results.
450

451 **Figure 3**

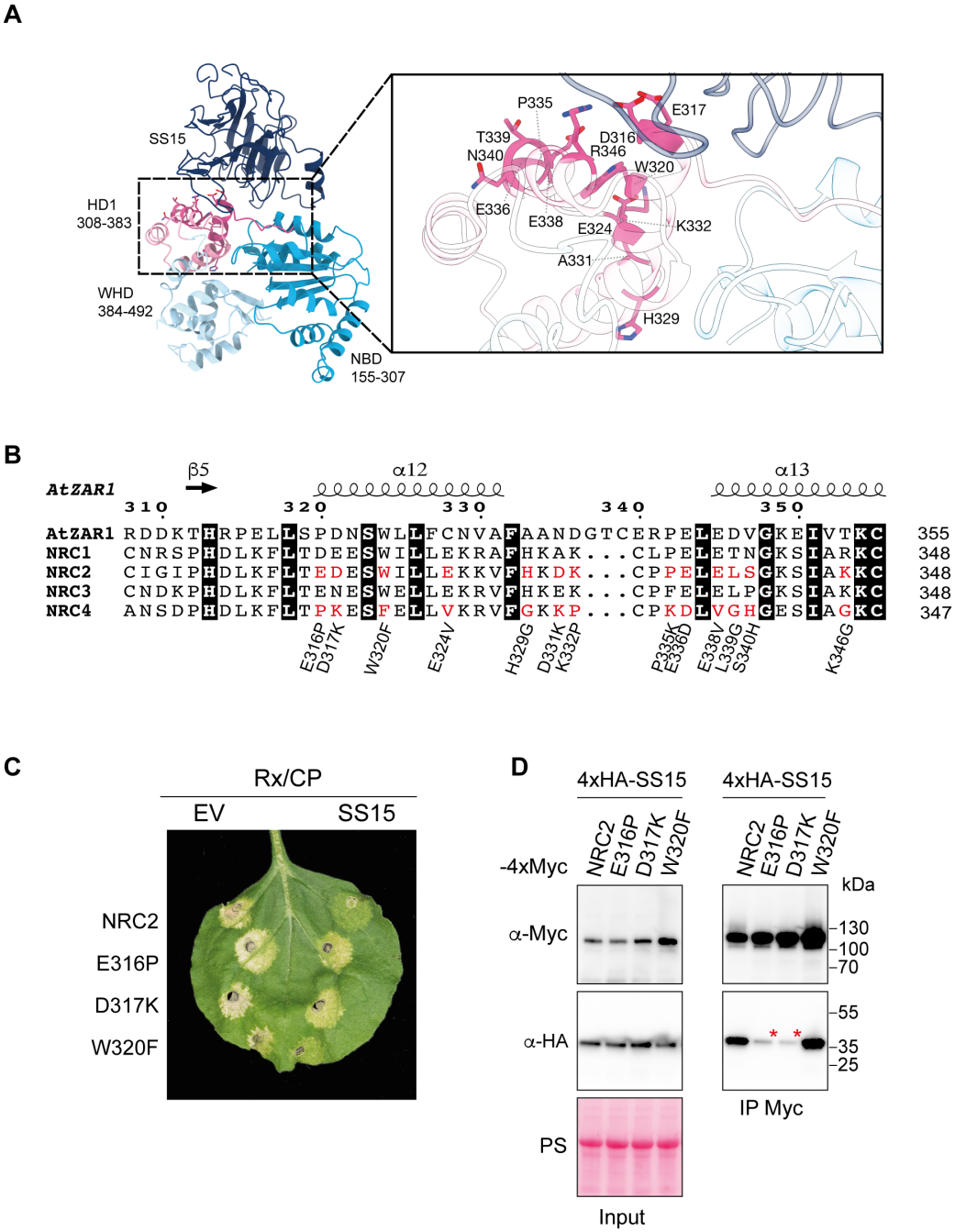

452

453 **Fig. 3: SS15-NRC binding interface enables bioengineering NRC2 variants that evade**
454 **suppression. (A)** Crystal structure of the SS15-SlNRC1^{NB-ARC} complex. The NB, HD1 and WHD
455 domains of SlNRC1^{NB-ARC} are shown in cyan, pale blue and magenta, respectively; SS15 is in dark blue.
456 The inset displays a close-up of the interface between SS15 and the HD1 domain of SlNRC1^{NB-ARC}
457 with the residues corresponding to those selected for mutagenesis in NRC2 highlighted in stick
458 representation. See **Table S3** for a summary of data collection and processing statistics. (**B**) Alignment

459 of HD1-1 region of AtZAR1, SlNRC1, NRC2, NRC3, and NRC4. Candidate residues (highlighted in
460 red) were shortlisted based on the interface identified in the co-crystal structure of SS15 and the
461 SlNRC1 NB-ARC domain, as well as being conserved in SlNRC1, NRC2 and NRC3 but not NRC4
462 and AtZAR1. 13 NRC2 variants were generated by mutating individual candidate positions to the
463 corresponding amino acid in NRC4 (detailed underneath the alignment). (**C**) Photo of representative
464 leaves from *N. benthamiana nrc2/3/4* KO plants showing HR after co-expression of Rx and PVX CP
465 with NRC2, or different NRC2 variants generated. These effector-sensor-helper combinations were
466 co-expressed with a free mCherry-6xHA fusion protein (EV) or with N-terminally 4xHA-tagged SS15.
467 The experiment consisted of 3 biological replicates. A quantitative analysis of HR phenotypes can be
468 found in **Fig. S7**. (**D**) Co-Immunoprecipitation (Co-IP) assays between SS15 and NRC2 variants. C-
469 terminally 4xMyc-tagged NRC2 variants were transiently co-expressed with N-terminally 4xHA-
470 tagged SS15. IPs were performed with agarose beads conjugated to Myc antibodies (Myc IP). While
471 only data for E316P, D317K and W320F NRC2 variants is shown, additional variants were also tested
472 and can be found in **Fig S6**. Total protein extracts were immunoblotted with appropriate antisera
473 labelled on the left. Approximate molecular weights (kDa) of the proteins are shown on the right.
474 Rubisco loading control was carried out using Ponceau stain (PS). The experiment was repeated three
475 times with similar results.
476

477 **Figure 4**

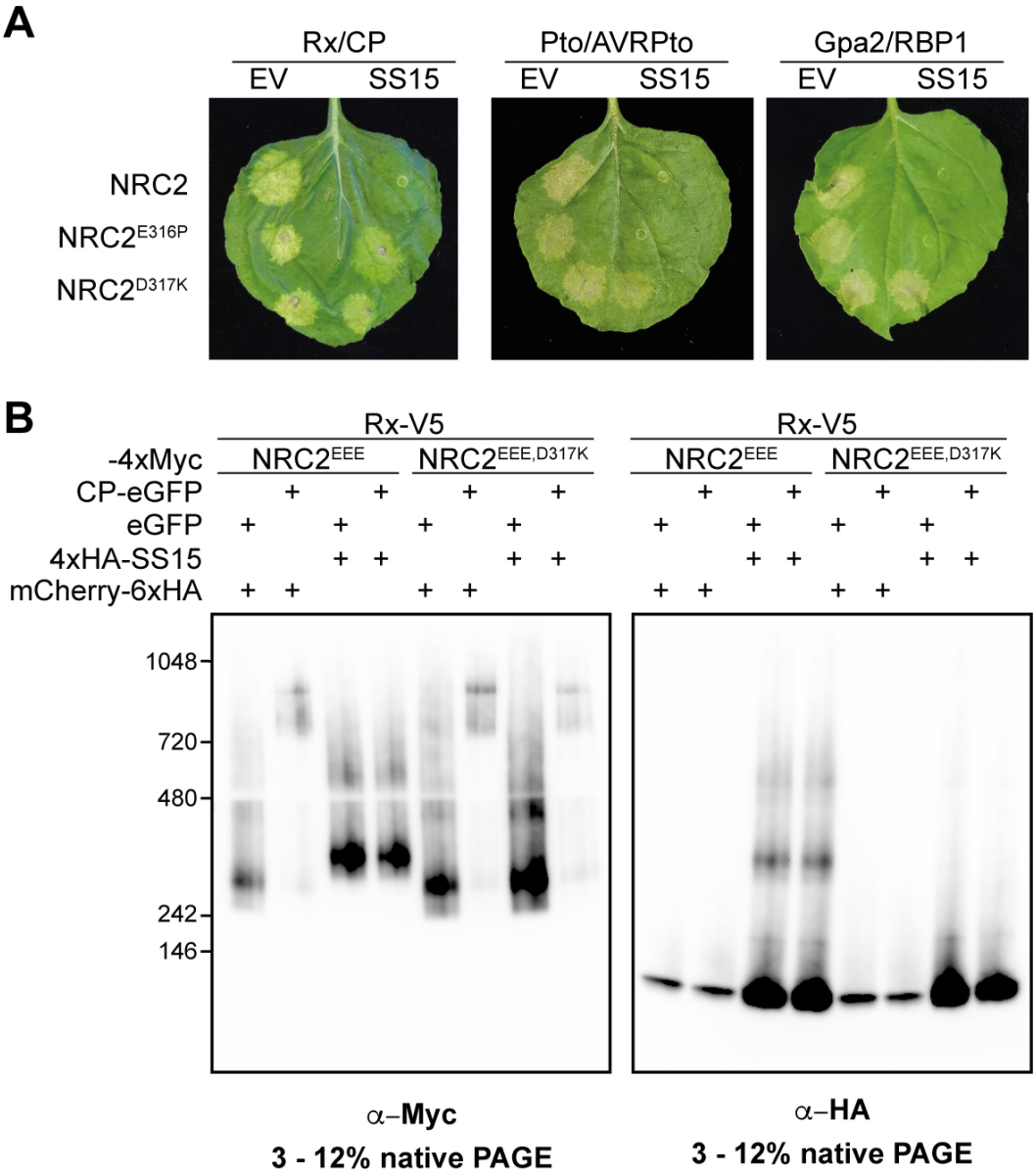

478

479 **Fig. 4: NRC2^{D317K} helper restores immune signaling of multiple disease resistance genes in**
480 **the presence of the effector SS15. (A)** Photo of representative leaves from *N. benthamiana nrc2/3/4*
481 KO plants showing HR after co-expression of Rx/CP, Pto/AVRPto or Gpa2/RBP1 together with
482 NRC2, NRC2^{E316P} or NRC2^{D317K} in the absence or presence of SS15. The experiment consisted of 3
483 biological replicates. A quantitative analysis of HR phenotypes can be found in **Fig. S8**. (**B**) BN-
484 PAGE assays with inactive and activated Rx together with NRC2 or NRC2^{D317K}, in the absence or
485 presence of SS15. C-terminally V5-tagged Rx and C-terminally 4xMyc-tagged NRC2^{EEE} or NRC2^{EEE-}
486 ^{D317K} were co-expressed with either free GFP or C-terminally GFP-tagged PVX CP. These effector-

487 sensor-helper combinations were co-infiltrated together with a 6xHA-mCherry fusion protein or with
488 N-terminally 4xHA-tagged SS15. Total protein extracts were run in parallel on native and denaturing
489 PAGE assays and immunoblotted with the appropriate antisera labelled below. Approximate
490 molecular weights (kDa) of the proteins are shown on the left. Corresponding SDS-PAGE blots can
491 be found in **Fig. S9**. The experiment was repeated three times with similar results.
492

493 **Supplemental Data**

494 **Figure S1**

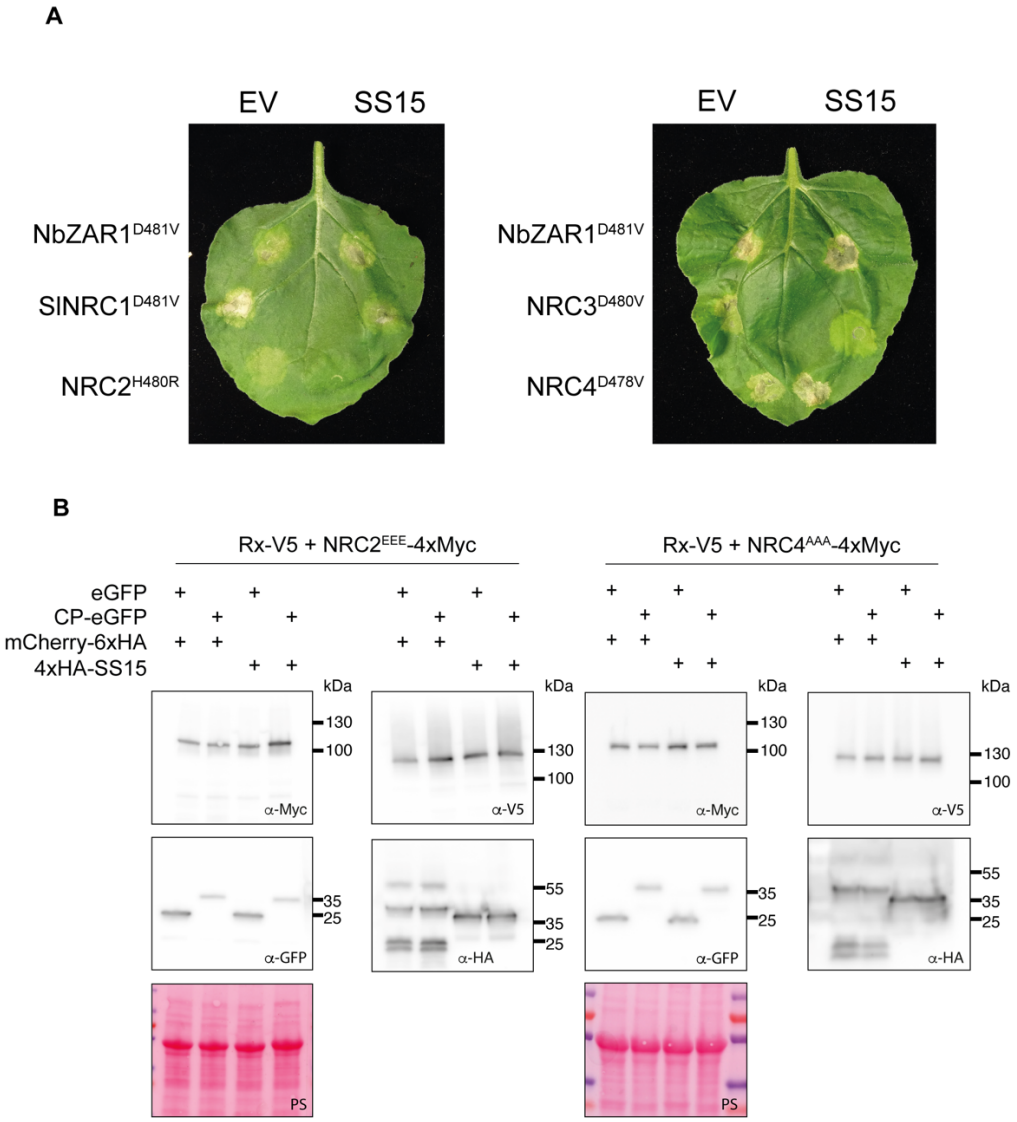

495

496 **Fig. S1: SS15 suppresses cell death mediated by SlNRC1, NRC2 and NRC3 but not NRC4 or**
497 **NbZAR1.**

498 (**A**) Photo of representative leaves from *N. benthamiana nrc2/3/4* KO plants showing HR after co-
499 expression of various autoactive NLR variants with a free mCherry-6xHA fusion protein (EV) or with
500 N-terminally 4xHA-tagged SS15. Images are representative of (**B**) SDS-PAGE accompanying BN-
501 PAGE shown in **Fig. 1B**. Total protein extracts were immunoblotted with the appropriate antisera
502 labelled on the left. Approximate molecular weights (kDa) of the proteins are shown on the right.
503 Rubisco loading control was carried out using Ponceau stain (PS). The experiment was repeated three
504 times with similar results.

505 # Figure S2

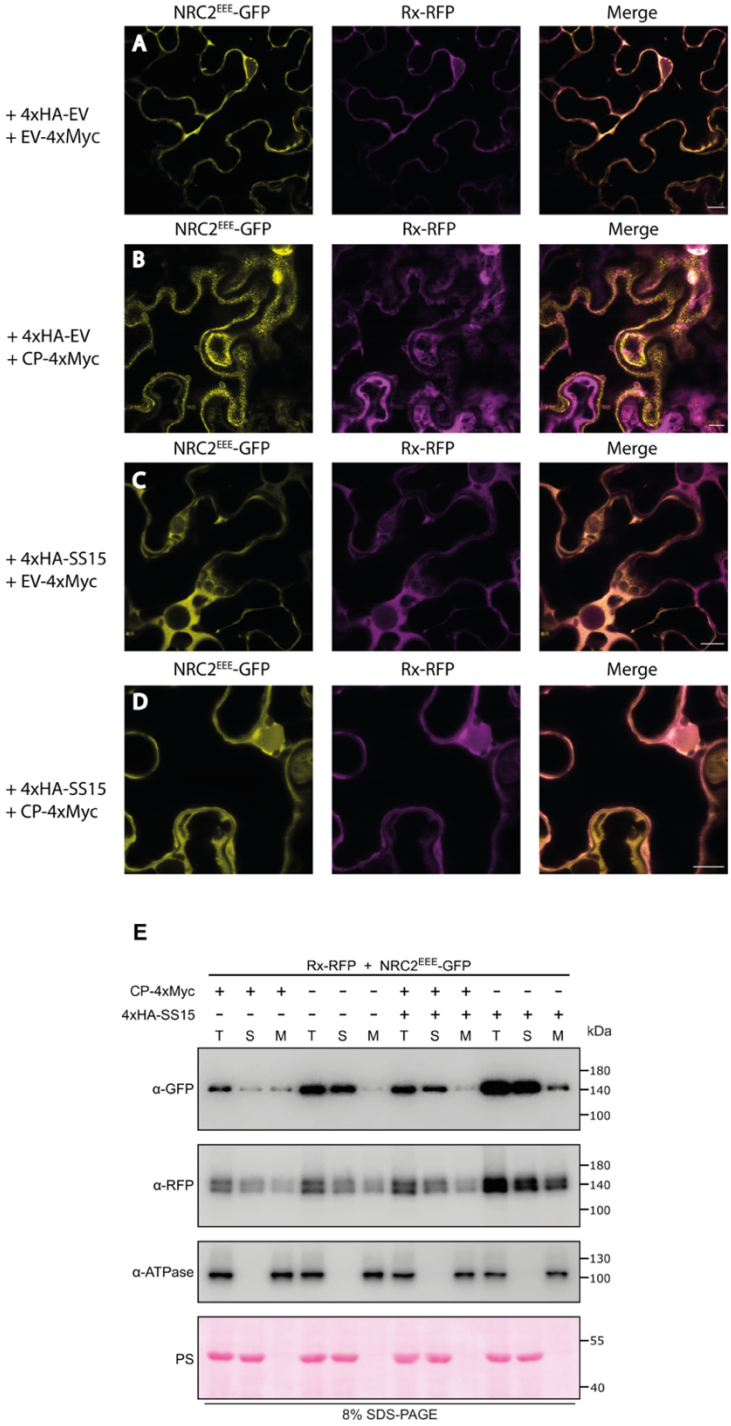

506

507 **Fig. S2: SS15 inhibits plasma membrane-association of activated NRC2.**

508 (**A-D**) C-terminally GFP-tagged NRC2^{EEE} and C-terminally RFP-tagged Rx were co-expressed with
509 an EV-4xMyc construct or a CP-4xMyc construct in leaves of *nrc2/3/4* KO *N. benthamiana*.
510 Representative single-plane confocal micrographs show the localization of both components of the

511 inactive and active Rx-NRC2 system. Scale bars represent 10 μm. (**A**) NRC2^{EEE}-GFP and Rx-RFP co-
512 localize in the cytoplasm. (**B**) As reported previously, Rx/CP activated NRC2^{EEE} forms plasma
513 membrane-associated puncta while Rx remains in the cytoplasm. (**C**) Co-expression with SS15 does
514 not alter the localization of inactive NRC2^{EEE}-GFP or Rx-RFP. (**D**) Upon co-expression CP-4xMyc,
515 Rx-RFP and NRC2^{EEE}-GFP with SS15, the punctate localization for NRC2^{EEE}-GFP is no longer
516 observed. (**E**) Membrane enrichment assays are consistent with microscopy. As reported previously,
517 inactive NRC2^{EEE}-GFP is mostly present in the soluble fraction (S) whereas activated NRC2^{EEE}-GFP
518 exhibits equal distribution across soluble and membrane (M) fractions. Upon co-expression with SS15,
519 NRC2^{EEE}-GFP distribution remains in the soluble fraction regardless of the presence or absence of
520 PVX CP. The experiment was repeated twice with similar results.
521

522 # Figure S3

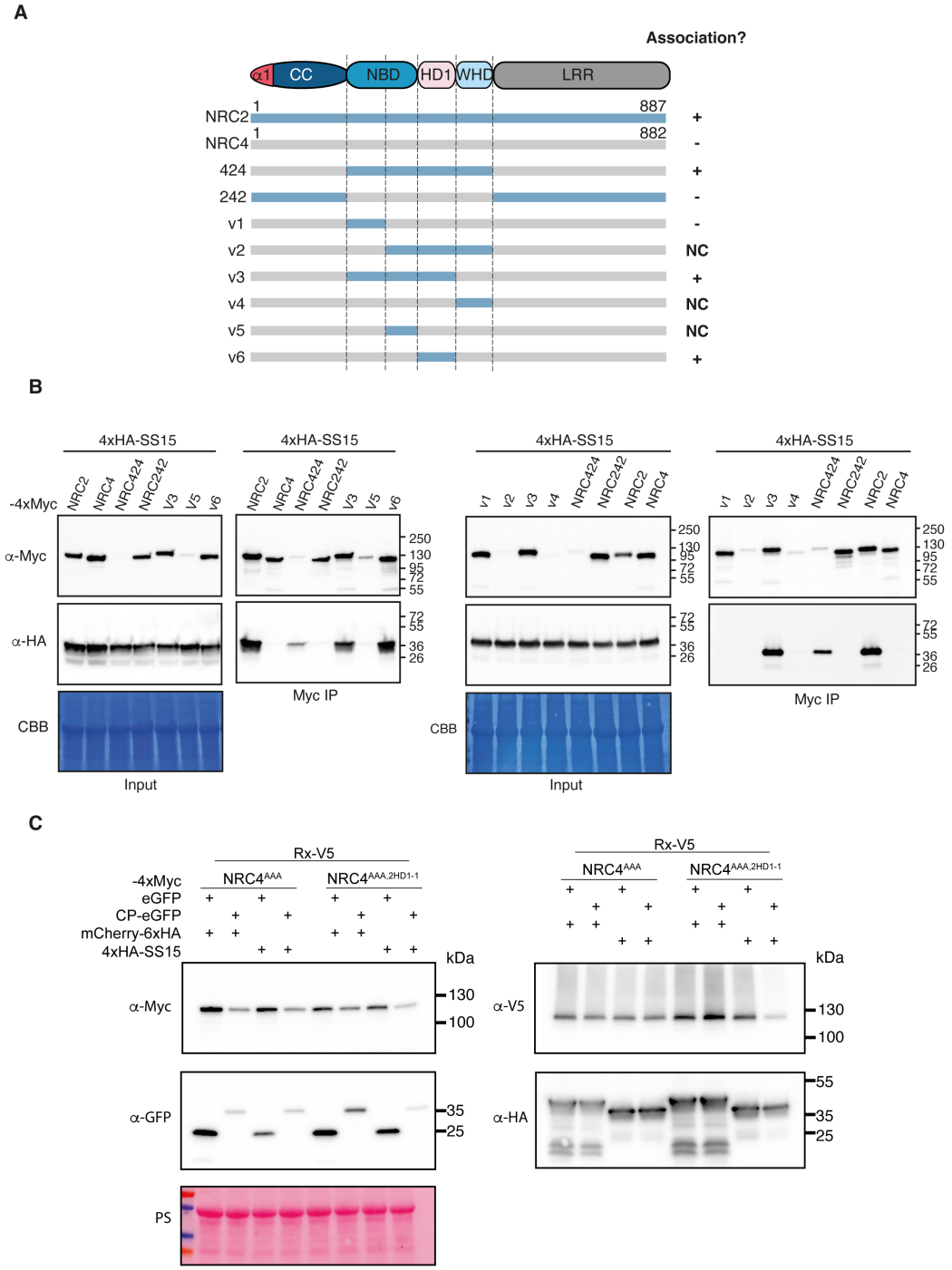

523

524 **Fig. S3: SS15 inhibits NRC2 by interacting with the HD1-1 region of the NB-ARC domain.**

525 **(A)** Schematic representation of all NRC2-NRC4 chimeric proteins generated. Association with SS15

526 (+) or lack thereof (-) is indicated on the right. (**B**) Co-Immunoprecipitation (Co-IP) assays between

527 SS15 and chimeric NRC2-NRC4 variants. C-terminally 4xMyc-tagged NRC proteins were transiently
528 co-expressed with N-terminally 4xHA-tagged SS15. IPs were performed with agarose beads
529 conjugated to Myc antibodies (Myc IP). Total protein extracts were immunoblotted with the
530 appropriate antisera labelled on the left. Approximate molecular weights (kDa) of the proteins are
531 shown on the right. Rubisco loading control was carried out using Ponceau stain (PS). The experiment
532 was repeated three times with similar results. (**C**) SDS-PAGE accompanying BN-PAGE shown in
533 **Fig. 2E**. Total protein extracts were immunoblotted with the appropriate antisera labelled on the left.
534 Approximate molecular weights (kDa) of the proteins are shown on the right. Rubisco loading control
535 was carried out using Ponceau stain (PS). The experiment was repeated three times with similar results.
536

537 # Figure S4

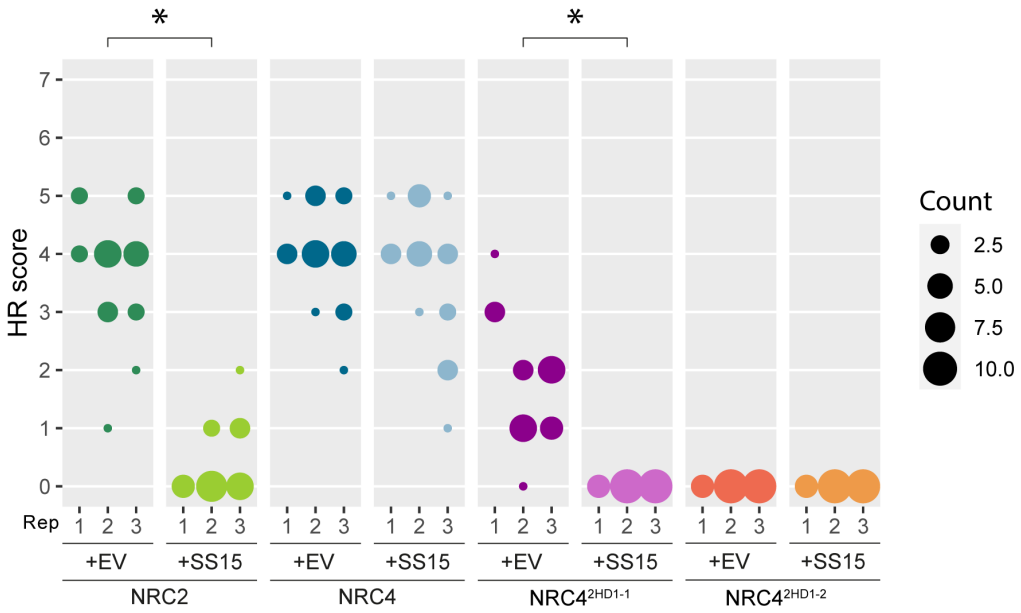

538

539 **Fig. S4: NRC4^{HD1-1} chimera is susceptible to inhibition by SS15.**

540 HR scores accompanying **Fig. 2D**. In all cases, Rx/CP was used to activate the system. HR was scored
541 based on a modified 0–7 scale (*49*) between 5–7 days post-infiltration. HR scores are presented as dot
542 plots, where the size of each dot is proportional to the number of samples with the same score (Count).
543 Results are based on 3 biological replicates. Statistical tests were implemented using the besthr R
544 library (*50*). We performed bootstrap resampling tests using a lower significance cut-off of 0.025 and
545 an upper cut-off of 0.975. Mean ranks of test samples falling outside of these cut-offs in the control
546 samples bootstrap population were considered significant. Significant differences between the
547 conditions are indicated with an asterisk (*).

548

549 **Figure S5**

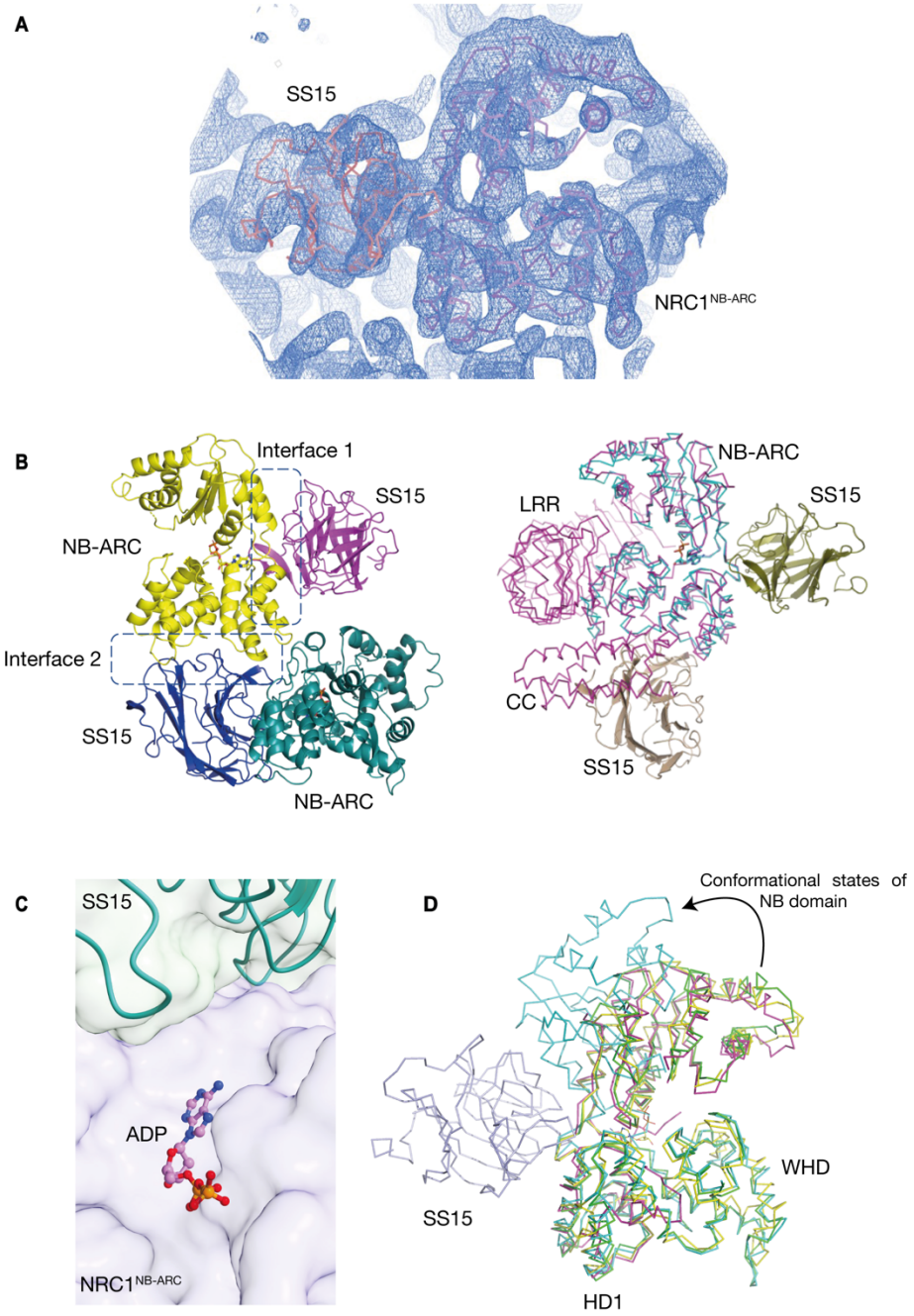

550

551 **Fig. S5: Crystal structure of SS15 in complex with SlNRC1$^{NB\text{-}ARC}$.**

552 Electron density map showing the relative orientation and arrangement of SS15 (orange) and
553 SlNRC1$^{NB\text{-}ARC}$ (violet) within an asymmetric unit. 2Fo-Fc map countered at 1σ **(B)** Two possible
554 interfaces between SS15 and SlNRC1$^{NB\text{-}ARC}$ revealed from the crystal packing. Both interfaces
555 (Interface 1 and Interface 2) are outlined (Left). Modelling of both potential binding interfaces for

556 SS15 complex with full length SlNRC1 (magenta) reveals a steric clash between the CC-domain of
557 SlNRC1 and SS15, making interface 2 unlikely to be biologically relevant in the full-length context
558 (Right). **(C)** Close up view of interaction between SS15-SlNRC1$^{NB\text{-}ARC}$ interaction interface relative to
559 the ATP-binding site within the NB-ARC domain of SlNRC1. The pyrophosphate moiety of ADP is
560 oriented facing opposite the SS15 binding interface (shown as ball and sticks), suggesting that SS15 is
561 unlikely to displace bound nucleotide or prevent ATP hydrolysis. **(D)** Structure of SS15-SlNRC1$^{NB\text{-}}$
562 ^{ARC} (yellow, PDB 8BV0) is superimposed over the NB-ARC domain of AtZAR1 in its inactive (green,
563 PDB 6J5W), intermediate (cyan, PDB 6J5V), and active resistosome (magenta, 6J5T) conformations.
564 Visualizing these three states reveals the trajectory of the NB domain as it moves relative to the HD1
565 and WHD domains while changing from inactive to activated states. The binding of SS15 at the critical
566 hinge region between the NB and HD1-WHD domains likely immobilizes this loop, preventing these
567 critical intramolecular rearrangements and therefore preventing NLR activation. See **Movie S1**.
568

569 **Figure S6**

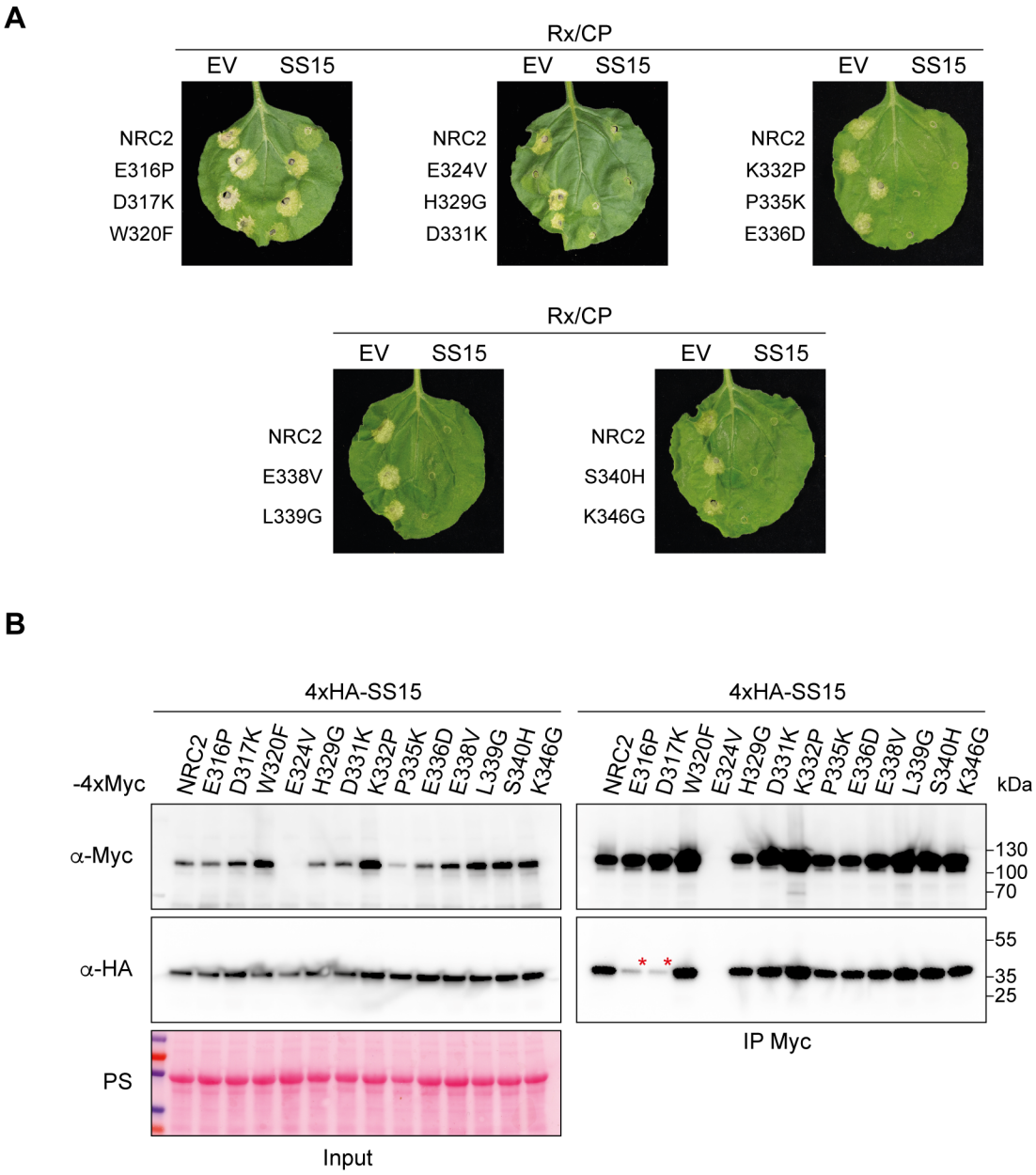

570

571

572 **Fig. S6: Out of 13 NRC2 variants tested, only E316P and D317K mutations abolish SS15**
573 **association and HR suppression. (A)** Photo of representative leaves from *N. benthamiana nrc2/3/4*
574 KO plants showing HR after co-expression of Rx and PVX CP with NRC2, or the different NRC2
575 variants generated. These effector-sensor-helper combinations were co-expressed with a free
576 mCherry-6xHA fusion protein (EV) or with N-terminally 4xHA-tagged SS15. (**B**) Co-
577 Immunoprecipitation (Co-IP) assays between SS15 and NRC2 variants. C-terminally 4xMyc-tagged

578 NRC2 variants were transiently co-expressed with N-terminally 4xHA-tagged SS15. IPs were
579 performed with agarose beads conjugated to Myc antibodies (Myc IP). Total protein extracts were
580 immunoblotted with appropriate antisera labelled on the left. Approximate molecular weights (kDa)
581 of the proteins are shown on the right. Rubisco loading control was carried out using Ponceau stain
582 (PS). The experiment was repeated three times with similar results.
583

584 # Figure S7

585

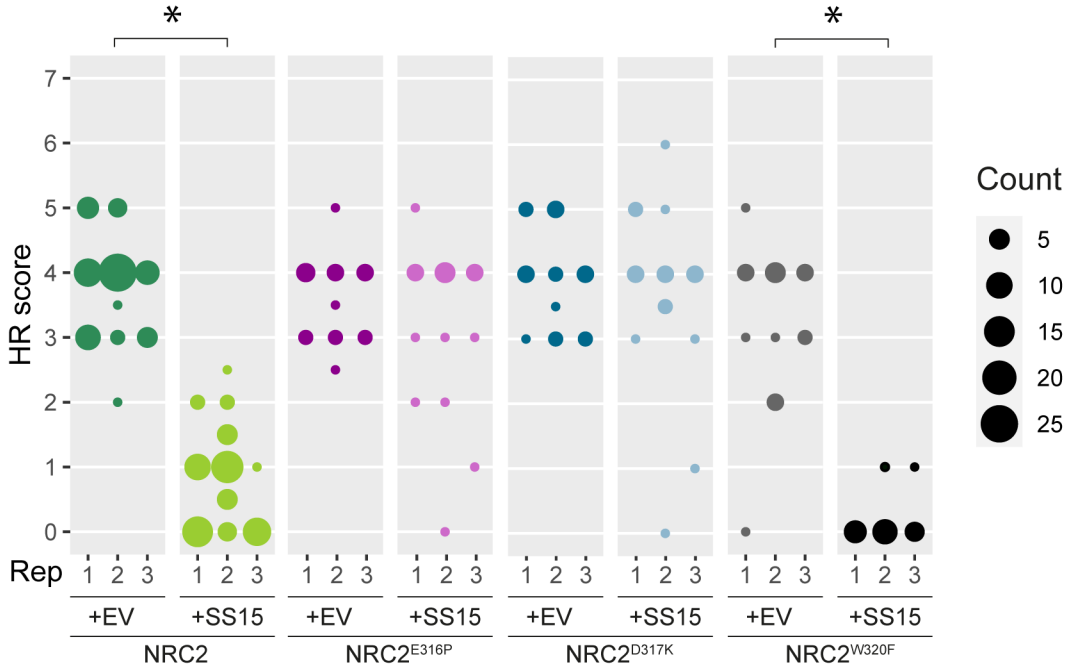

586

587 **Fig. S7: NRC2^{E316P} and NRC2^{D317K} abolish SS15-mediated suppression of Rx.**

588 HR scores accompanying **Fig. 3C**. In all cases, Rx/CP was used to activate the system. HR was scored
589 based on a modified 0–7 scale (*49*) between 5–7 days post-infiltration. HR scores are presented as dot
590 plots, where the size of each dot is proportional to the number of samples with the same score (Count).
591 Results are based on 3 biological replicates. Statistical tests were implemented using the besthr R
592 library (*50*). We performed bootstrap resampling tests using a lower significance cut-off of 0.025 and
593 an upper cut-off of 0.975. Mean ranks of test samples falling outside of these cut-offs in the control
594 samples bootstrap population were considered significant. Significant differences between the
595 conditions are indicated with an asterisk (*).

596

597 # Figure S8

598

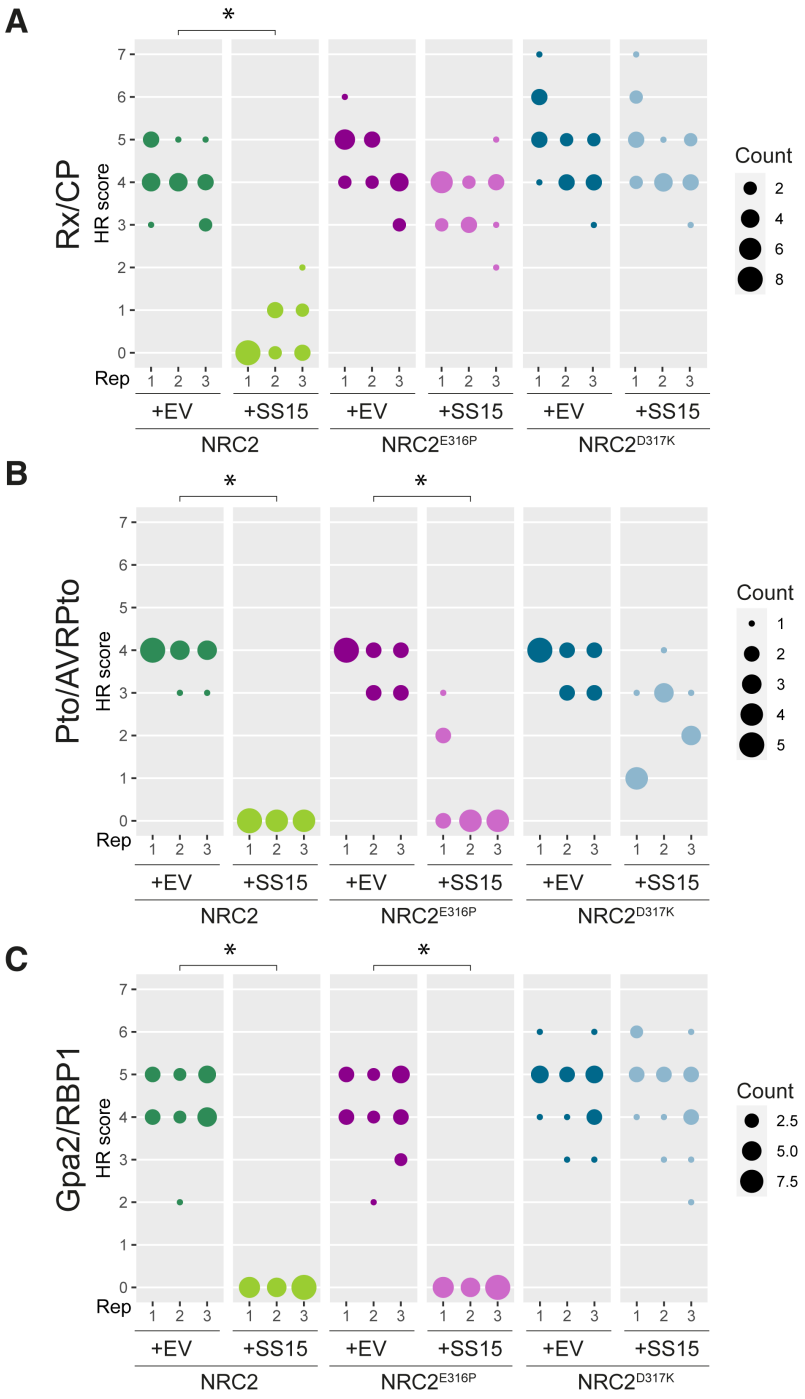

599

600 **Fig. S8: NRC2^{D317K} abolishes SS15-mediated suppression of Rx, Gpa2 and Prf.**

601 HR scores accompanying **Fig. 4A**. NRCs were activated using Rx/CP (**A**), Pto/AVRPto (**B**) or

602 Gpa2/RBP1 (**C**). HR was scored based on a modified 0–7 scale (*49*) between 5–7 days post-

603 infiltration. HR scores are presented as dot plots, where the size of each dot is proportional to the
604 number of samples with the same score (count). Results are based on 3 biological replicates. Statistical
605 tests were implemented using the besthr R library (*50*). We performed bootstrap resampling tests using
606 a lower significance cut-off of 0.025 and an upper cut-off of 0.975. Mean ranks of test samples falling
607 outside of these cut-offs in the control samples bootstrap population were considered significant.
608 Significant differences between the conditions are indicated with an asterisk (*).

609 **Figure S9**

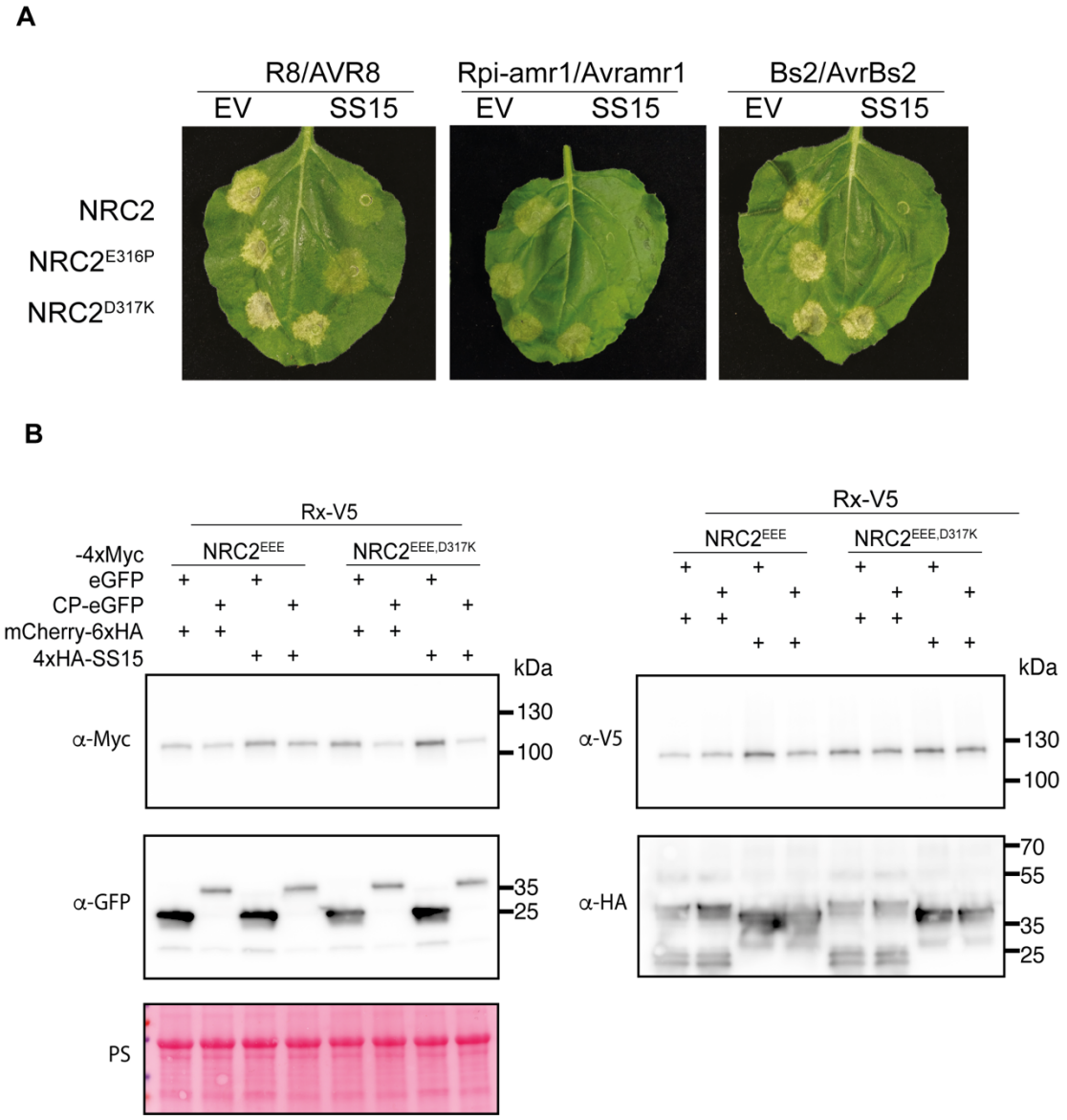

610

611 **Fig. S9: NRC2^{D317K} abolishes SS15-mediated suppression of all NRC2-dependent sensors**
612 **tested and restores NRC2 resistosome formation.**

613 Photo of representative leaves from *N. benthamiana nrc2/3/4* KO plants showing HR after co-
614 expression of NRC2, or different NRC2 variants generated with various sensor/effector pairs. These
615 effector-sensor-helper combinations were co-expressed with a free mCherry-6xHA fusion protein
616 (EV) or with N-terminally 4xHA-tagged SS15. (**B**) SDS-PAGE accompanying BN-PAGE shown in
617 **Fig. 4B**. Total protein extracts were immunoblotted with the appropriate antisera labelled on the left.
618 Approximate molecular weights (kDa) of the proteins are shown on the right. Rubisco loading control
619 was carried out using Ponceau stain (PS). The experiment was repeated three times with similar results.

620 ## Supplementary Tables

621 **Table S1: List of constructs used in this study.** (As separate file)

622 **Table S2: List of OD_{600} used for agroinfiltration experiments.** (As separate file)

623 **Table S3: Summary of X-ray data and model parameters for NRC1-SS15.**

624

Data collection	
Diamond Light Source beamline	I03
Wavelength (Å)	0.9763
Detector	Eiger2 XE 16M
Resolution range (Å)	51.34 – 4.50 (5.03 – 4.50)
Space Group	$P6_1$
Cell parameters (Å)	$a = b = 128.6$, $c = 170.7$
Total no. of measured intensities	77102 (13865)
Unique reflections	8981 (2263)
Multiplicity	8.6 (6.1)
Mean $I/\sigma(I)$	7.2 (1.5)
Completeness (%)	94.0 (84.0)
R_{merge}[a]	0.084 (1.513)
R_{meas}[b]	0.033 (0.612)
$CC_{½}$[c]	0.998 (0.588)
Refinement	
Resolution range (Å)	51.34 – 4.50 (4.62 – 4.50)
Reflections: working/free[d]	8075/883
R_{work}/ R_{free}[e]	0.237/0.275
MolProbity score/Clashscore[f]	1.58/5.41
Ramachandran plot: favoured/allowed/disallowed[f] (%)	95.9/4.1/0.0
R.m.s. bond distance deviation (Å)	0.003
R.m.s. bond angle deviation (°)	0.79
NRC1 – chains/no. protein residues/ranges	A,C/343/153-494
SS15 – chains/no. protein residues/ranges	B,D/206/18-223
No. ADP molecules/RSCC[g]	2/0.72,0.84

PDB accession code	8BV0

Values in parentheses are for the outer resolution shell.

[a] $R_{merge} = \sum_{hkl} \sum_{I} | I_i(hkl) - \langle I(hkl) \rangle | / \sum_{hkl} \sum_i I_i(hkl)$.

[b] $R_{meas} = \sum_{hkl} [N/(N-1)]^{1/2} \times \sum_{I} | I_i(hkl) - \langle I(hkl) \rangle | / \sum_{hkl} \sum_i I_i(hkl)$, where $I_i(hkl)$ is the ith observation of reflection hkl, $\langle I(hkl) \rangle$ is the weighted average intensity for all observations I of reflection hkl and N is the number of observations of reflection hkl.

[c] $CC_{½}$ is the correlation coefficient between symmetry equivalent intensities from random halves of the dataset.

[d] The data set was split into "working" and "free" sets consisting of 90 and 10% of the data respectively. The free set was not used for refinement.

[e] The R-factors R_{work} and R_{free} are calculated as follows: $R = \sum(| F_{obs} - F_{calc} |)/\sum| F_{obs} |$, where F_{obs} and F_{calc} are the observed and calculated structure factor amplitudes, respectively.

[f] As calculated using MolProbity (*51*).

[g] Real Space Correlation Coefficient as calculated by the PDB validation server.

Supplementary Movies

Movie S1: SS15 immobilizes hinge region between NB and HD1-WHD domains of NRCs to prevent NLR activation.

Acknowledgements

We are very thankful to Jiorgos Kourelis, Clemence Marchal, Daniel Lüdke and Hee-Kyung Ahn (The Sainsbury Laboratory, Norwich, UK) for invaluable scientific discussions, ideas, and feedback. We thank Julia Mundy for assistance with crystallography experiments. We thank the Diamond Light Source, UK (beamline i03 under proposal MX18565) for access to X-ray data collection facilities. M.P.C. thanks Emiliano "Dibu" Martínez and Lionel Messi for inspiration. We thank all members of the TSL Support Services for their invaluable assistance.

Funding:

The Kamoun Lab is funded primarily from the Gatsby Charitable Foundation, Biotechnology and Biological Sciences Research Council (BBSRC, UK, BB/WW002221/1, BB/V002937/1, BBS/E/J/000PR9795 and BBS/E/J/000PR9796) and the European Research Council (BLASTOFF).

Author Contributions:

Conceptualization: M.P.C, C-H.W., S.K., L.D.

Methodology: M.P.C., H.P., M.S., D.M.L., C.E.M.S., L.D.

Validation: M.P.C., H.P., M.S., Y.T., C.D., E.L.H.Y., A.H.

Formal Analysis: M.P.C., H.P., M.S., A.T., D.M.L., Y.T., C.D., C.E.M.S.

Investigation: M.P.C., H.P., M.S., Y.T., C.D., E.L.H.Y., A.H., L.D.

Data Curation: M.P.C., H.P., M.S., A.T., D.M.L., Y.T., C.D., E.L.H.Y., C.E.M.S., A.H.

Visualization: M.P.C., H.P., M.S., A.T., Y.T., C.D., E.L.H.Y., L.D.

Writing – Original Draft: M.P.C., S.K., L.D.

Writing – Review & Editing: M.P.C., D.M.L., S.K., L.D.

Supervision: M.P.C., T.O.B., S.K., L.D.

Project Administration: M.P.C., T.O.B., S.K., L.D.

Funding Acquisition: T.O.B., S.K., L.D.

Competing interests:

C.D., T.O.B and S.K. receive funding from industry on NLR biology. M.P.C., S.K. and L.D. have filed patents on NLR biology.

674 **Data and materials availability:**

675 All relevant data are within the paper, in the Supplementary Materials and Source Data files. Data
676 relevant to the structure presented in **Fig. 3** can be found in the Protein Data Bank, PDB 8BV0.

677

678 ## References

679

680 1. J. D. Jones, R. E. Vance, J. L. Dangl, Intracellular innate immune surveillance devices in
681 plants and animals. *Science* **354**, aaf6395 (2016).
682 2. Z. Duxbury, C.-h. Wu, P. Ding, A comparative overview of the intracellular guardians of
683 plants and animals: NLRs in innate immunity and beyond. *Annual review of plant biology*
684 **72**, 155-184 (2021).
685 3. J. Wang *et al.*, Reconstitution and structure of a plant NLR resistosome conferring
686 immunity. *Science* **364**, eaav5870 (2019).
687 4. M. P. Contreras *et al.*, Sensor NLR immune proteins activate oligomerization of their NRC
688 helpers in response to plant pathogens. *The EMBO Journal,* e111519 (2022).
689 5. H.-K. Ahn *et al.*, Effector-dependent activation and oligomerization of plant NRC class
690 helper NLRs by sensor NLR immune receptors Rpi-amr3 and Rpi-amr1. *The EMBO Journal,*
691 e111484 (2023).
692 6. A. Förderer *et al.*, A wheat resistosome defines common principles of immune receptor
693 channels. *bioRxiv*, 2022.2003.2023.485489 (2022).
694 7. R. Martin *et al.*, Structure of the activated ROQ1 resistosome directly recognizing the
695 pathogen effector XopQ. *Science* **370**, eabd9993 (2020).
696 8. I. V. Hochheiser *et al.*, Structure of the NLRP3 decamer bound to the cytokine release
697 inhibitor CRID3. *Nature* **604**, 184-189 (2022).
698 9. Z. Hu *et al.*, Structural and biochemical basis for induced self-propagation of NLRC4.
699 *Science* **350**, 399-404 (2015).
700 10. Z. Duxbury *et al.*, Induced proximity of a TIR signaling domain on a plant-mammalian NLR
701 chimera activates defense in plants. *Proceedings of the National Academy of Sciences* **117**,
702 18832-18839 (2020).
703 11. B. P. M. Ngou, P. Ding, J. D. Jones, Thirty years of resistance: Zig-zag through the plant
704 immune system. *The Plant Cell* **34**, 1447-1478 (2022).
705 12. L. A. Gao *et al.*, Prokaryotic innate immunity through pattern recognition of conserved
706 viral proteins. *Science* **377**, eabm4096 (2022).
707 13. C.-H. Wu, L. Derevnina, S. Kamoun, Receptor networks underpin plant immunity. *Science*
708 **360**, 1300-1301 (2018).
709 14. L. D. Cunha *et al.*, Inhibition of inflammasome activation by Coxiella burnetii type IV
710 secretion system effector IcaA. *Nature communications* **6**, 1-13 (2015).
711 15. L. Derevnina *et al.*, Plant pathogens convergently evolved to counteract redundant nodes
712 of an NLR immune receptor network. *PLoS biology* **19**, e3001136 (2021).
713 16. H. Yen, N. Sugimoto, T. Tobe, Enteropathogenic Escherichia coli uses NleA to inhibit NLRP3
714 inflammasome activation. *PLoS pathogens* **11**, e1005121 (2015).

715 17. Q. Chai *et al.*, A bacterial phospholipid phosphatase inhibits host pyroptosis by hijacking
716 ubiquitin. *Science* **378**, eabq0132 (2022).
717 18. C. Marchal, H. Pai, S. Kamoun, J. Kourelis, Emerging principles in the design of
718 bioengineered made-to-order plant immune receptors. *Current Opinion in Plant Biology*,
719 102311 (2022).
720 19. J. Kourelis, T. Sakai, H. Adachi, S. Kamoun, RefPlantNLR is a comprehensive collection of
721 experimentally validated plant disease resistance proteins from the NLR family. *PLoS*
722 *Biology* **19**, e3001124 (2021).
723 20. H. Adachi, L. Derevnina, S. Kamoun, NLR singletons, pairs, and networks: evolution,
724 assembly, and regulation of the intracellular immunoreceptor circuitry of plants. *Current*
725 *opinion in plant biology* **50**, 121-131 (2019).
726 21. C.-H. Wu *et al.*, NLR network mediates immunity to diverse plant pathogens. *Proceedings*
727 *of the National Academy of Sciences* **114**, 8113-8118 (2017).
728 22. C. N. LaRock, B. T. Cookson, The Yersinia virulence effector YopM binds caspase-1 to arrest
729 inflammasome assembly and processing. *Cell host & microbe* **12**, 799-805 (2012).
730 23. H. Chen *et al.*, The bacterial T6SS effector EvpP prevents NLRP3 inflammasome activation
731 by inhibiting the Ca2+-dependent MAPK-Jnk pathway. *Cell host & microbe* **21**, 47-58
732 (2017).
733 24. H. S. Karki, S. Abdullah, Y. Chen, D. A. Halterman, Natural genetic diversity in the potato
734 resistance gene RB confers suppression avoidance from Phytophthora effector IPI-O4.
735 *Molecular Plant-Microbe Interactions* **34**, 1048-1056 (2021).
736 25. H. Adachi *et al.*, An N-terminal motif in NLR immune receptors is functionally conserved
737 across distantly related plant species. *Elife* **8**, e49956 (2019).
738 26. J. Kourelis *et al.*, The helper NLR immune protein NRC3 mediates the hypersensitive cell
739 death caused by the cell-surface receptor Cf-4. *bioRxiv*, (2021).
740 27. J. Wang *et al.*, Ligand-triggered allosteric ADP release primes a plant NLR complex. *Science*
741 **364**, eaav5868 (2019).
742 28. J. Kourelis, C. Marchal, S. Kamoun, NLR immune receptor-nanobody fusions confer plant
743 disease resistance. *bioRxiv*, (2021).
744 29. E. Weber, C. Engler, R. Gruetzner, S. Werner, S. Marillonnet, A modular cloning system for
745 standardized assembly of multigene constructs. *PloS one* **6**, e16765 (2011).
746 30. C. Engler *et al.*, A golden gate modular cloning toolbox for plants. *ACS synthetic biology* **3**,
747 839-843 (2014).
748 31. M. P. Contreras *et al.*, Sensor NLR immune proteins activate oligomerization of their NRC
749 helper. *BioRxiV*, (2022).
750 32. L. Derevnina *et al.*, Plant pathogens convergently evolved to counteract redundant nodes
751 of an NLR immune receptor network. *PLoS biology* **19**, e3001136 (2021).
752 33. C. Duggan *et al.*, Dynamic localization of a helper NLR at the plant–pathogen interface
753 underpins pathogen recognition. *Proceedings of the National Academy of Sciences* **118**,
754 (2021).
755 34. L. Abas, C. Luschnig, Maximum yields of microsomal-type membranes from small amounts
756 of plant material without requiring ultracentrifugation. *Analytical biochemistry* **401**, 217-
757 227 (2010).

758 35. F. W. Studier, Protein production by auto-induction in high-density shaking cultures.
759 *Protein expression and purification* **41**, 207-234 (2005).
760 36. J. F. Steele, R. K. Hughes, M. J. Banfield, Structural and biochemical studies of an NB-ARC
761 domain from a plant NLR immune receptor. *PLoS One* **14**, e0221226 (2019).
762 37. W. Kabsch, xds. *Acta Crystallographica Section D: Biological Crystallography* **66**, 125-132
763 (2010).
764 38. G. Winter, xia2: an expert system for macromolecular crystallography data reduction.
765 *Journal of applied crystallography* **43**, 186-190 (2010).
766 39. P. R. Evans, G. N. Murshudov, How good are my data and what is the resolution? *Acta*
767 *Crystallographica Section D: Biological Crystallography* **69**, 1204-1214 (2013).
768 40. M. Winn, An overview of the CCP4 project in protein crystallography: an example of a
769 collaborative project. *Journal of synchrotron radiation* **10**, 23-25 (2003).
770 41. R. Evans *et al.*, Protein complex prediction with AlphaFold-Multimer. *bioRxiv*,
771 2021.2010.2004.463034 (2022).
772 42. M. Mirdita *et al.*, ColabFold: making protein folding accessible to all. *Nature Methods*, 1-
773 4 (2022).
774 43. A. J. McCoy *et al.*, Phaser crystallographic software. *Journal of applied crystallography* **40**,
775 658-674 (2007).
776 44. P. Emsley, B. Lohkamp, W. G. Scott, K. Cowtan, Features and development of Coot. *Acta*
777 *Crystallographica Section D: Biological Crystallography* **66**, 486-501 (2010).
778 45. G. N. Murshudov *et al.*, REFMAC5 for the refinement of macromolecular crystal
779 structures. *Acta Crystallographica Section D: Biological Crystallography* **67**, 355-367
780 (2011).
781 46. R. A. Nicholls, M. Fischer, S. McNicholas, G. N. Murshudov, Conformation-independent
782 structural comparison of macromolecules with ProSMART. *Acta Crystallographica Section*
783 *D: Biological Crystallography* **70**, 2487-2499 (2014).
784 47. E. F. Pettersen *et al.*, UCSF ChimeraX: Structure visualization for researchers, educators,
785 and developers. *Protein Science* **30**, 70-82 (2021).
786 48. The PyMOL Molecular Graphics System, Version 1.2r3pre, Schrödinger, LLC.
787 49. M. E. Segretin *et al.*, Single amino acid mutations in the potato immune receptor R3a
788 expand response to Phytophthora effectors. *Molecular Plant-Microbe Interactions* **27**,
789 624-637 (2014).
790 50. D. MacLean, Besthr. *Zenodo*, (2019).
791 51. I. W. Davis *et al.*, MolProbity: all-atom contacts and structure validation for proteins and
792 nucleic acids. *Nucleic acids research* **35**, W375-W383 (2007).
793